

Geology and in situ stress of the MH-2 borehole, Idaho, USA: Insights into western Snake River Plain structure from geothermal exploration drilling

J.A. Kessler^{1,*}, K.K. Bradbury¹, J.P. Evans¹, M.A. Pulsipher¹, D.R. Schmitt², J.W. Shervais¹, F.E. Rowe¹, and J. Varriale^{1,†}

¹DEPARTMENT OF GEOLOGY, UTAH STATE UNIVERSITY, 4505 OLD MAIN HILL, LOGAN, UTAH 84322, USA

²DEPARTMENT OF PHYSICS, UNIVERSITY OF ALBERTA, 4-181 CCIS, EDMONTON, ALBERTA T6G 2E1, CANADA

ABSTRACT

Project HOTSPOT, the Snake River Scientific Drilling Project (International Continental Scientific Drilling Program), tested for deep geothermal resources and examined the petrology of volcanic rocks with three drillholes in the central and western Snake River Plain (western USA). The MH-2 drillhole targeted fractured crystalline and hydrothermally altered basalt in the area of the Mountain Home Air Force Base (Idaho) to a total depth of 1821 m. At 1745 m depth the drillhole encountered flowing artesian hydrothermal fluids of at least 150 °C. We integrate geological analyses of core, image log, and borehole geophysical data, and in situ stress analyses to describe the structural environment that produces permeability for artesian flow. The rocks in the lower 540 m of the drillhole consist of basalt flows as much as 30 m thick, altered basalt, and thin sedimentary horizons. The mechanical stratigraphy is defined by nine mechanical horizons that are in three ranges of rock strength on the basis of experimentally determined strength data, core logging, and geophysical log signatures. Hydrothermal alteration products and mineralization in the core are associated with three highly faulted sections; the lowermost section is associated with the zone of flowing thermal water. Shear slip indicators on faults observed in core indicate slip ranging from pure strike slip to normal failure mechanisms in the stronger horizons. The borehole breakouts indicate that the maximum horizontal stress, S_H , is oriented $047^\circ \pm 7^\circ$, and drilling-induced tensile fractures indicate that S_H is oriented at $67^\circ \pm 21^\circ$. The in situ stress orientations exhibit little variation over the depth of the measured interval, but the S_H magnitude varies with depth, and is best explained by an oblique normal fault stress regime. The geomechanical model indicates that if pore pressures at depth are elevated above the normal hydrostatic gradient, as observed here, the system has the potential to deform by mixed normal and strike-slip failure. Our observations and interpretations suggest that the MH-2 borehole was drilled into oblique normal faults that intersect a buried 300° -trending fault block masked by the basaltic volcanic complex. These data indicate that the transition from the central to western Snake River Plain is characterized by complex structures developed in response to a transitional stress state related to Snake River Plain and western Basin and Range stress regimes. The western Basin and Range stress and tectonic regime may extend from northern Nevada into western Idaho and may enhance the potential for geothermal resources by creating interconnected fracture and fault-related permeability at depth.

LITHOSPHERE, v. 9, no. 3, p. 476–498; GSA Data Repository Item 2017171 | Published online 4 April 2017

doi:10.1130/L609.1

INTRODUCTION

The Snake River Scientific Drilling Project (International Continental Scientific Drilling Program, Project HOTSPOT) examined the potential for the presence of commercial geothermal energy resources in the central and western portions of the Snake River Plain (SRP; Idaho, USA) (Nielsen et al., 2012, 2014; Shervais, 2014;

Shervais et al., 2013, 2014a, 2014b). Three boreholes were drilled to examine the geothermal gradient, in situ fluid chemistry and temperature, core geochemistry and lithology, geomechanical properties of the core, and borehole stress states at sites that exhibit potential for geothermal resources. Borehole MH-2 was drilled to a total depth (TD) of 1821 m in the western SRP on the Mountain Home Air Force Base (MHAFB), near Mountain Home, Idaho (Fig. 1) to explore the potential of basalt-hosted geothermal systems below a thick stratigraphic section of lacustrine deposits (Shervais et al., 2013).

Basalt-hosted geothermal systems rely on connected fracture and fault networks for fluid storage and permeability (Kinslow et al., 2012).

Connected fractures provide the volume for fluid storage, the mechanism of advective heat transfer in the fluids, and the permeability required for convective heat transfer and production from the reservoir (Wohletz and Heiken, 1992). In some cases, as few as 10%–20% of the fractures appear to provide connected pathways for flow (Morin et al., 1997). Any characterization of a basalt-hosted geothermal system must therefore identify, describe, and model the fracture pathways. At depth, fracture permeability is a function of aperture, remnant porosity, strength of fill minerals, elastic properties of the host rock, and orientation of fractures relative to the modern stress state.

An integrated analysis of borehole geophysical data, core, alteration chemistry and petrology,

Corresponding author: James Evans  <http://orcid.org/0000-0002-2181-3866>

*Present address: Occidental Petroleum Corporation, 5 Greenway Plaza, Houston, Texas 77046, USA

†Present address: Anadarko Petroleum Company, 1201 Lake Robbins Drive, The Woodlands, Texas 77380, USA

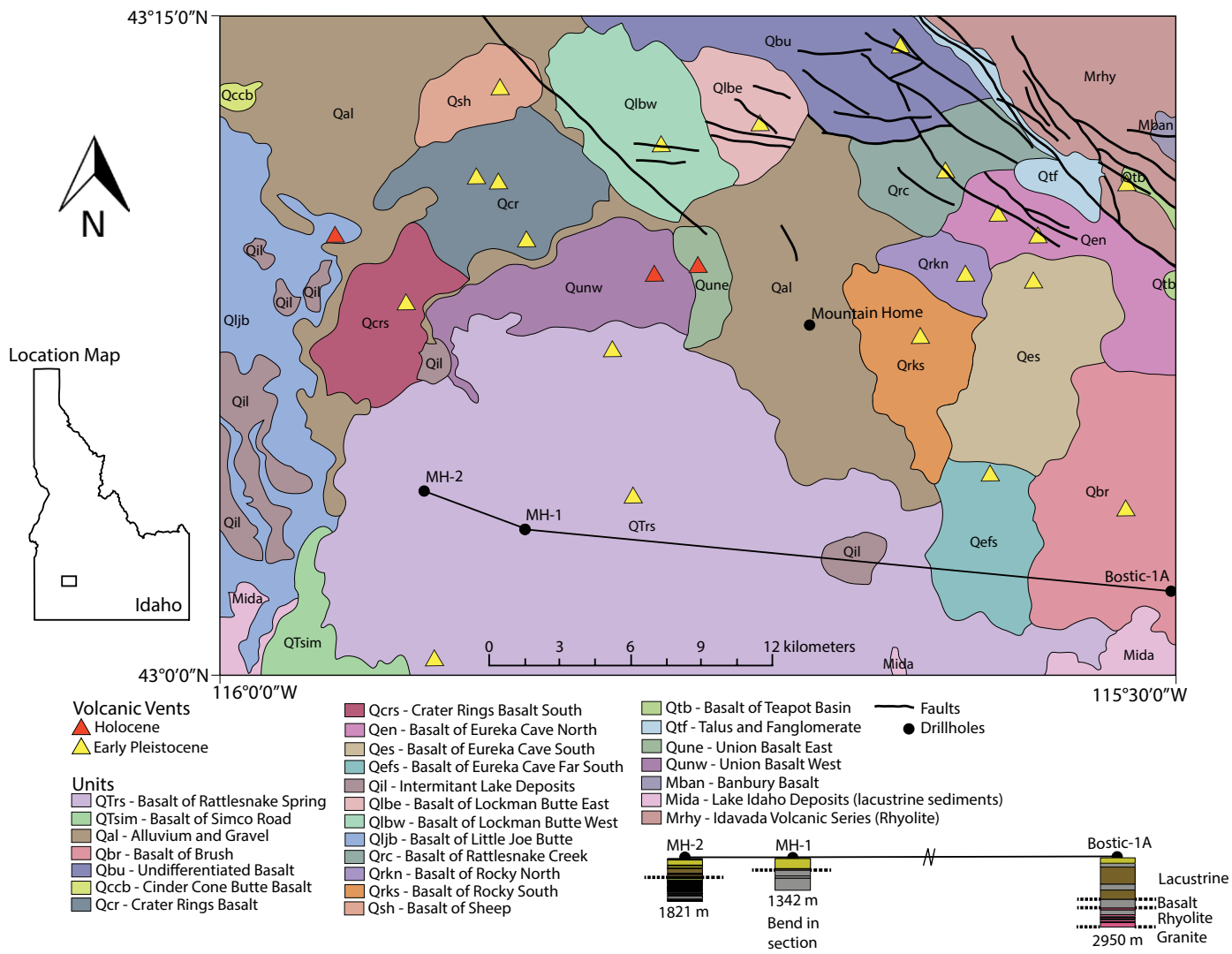


Figure 1. Generalized geologic map of the Mountain Home drill site and surrounding region, Snake River Plain, Idaho. The area is dominated by Quaternary (Q) basalt flows and west-northwest–striking faults along the northern margin of the area. Major volcanic vents and the location of key boreholes are also shown. (Map data are from Shervais et al., 2005 and Shervais and Vetter, 2009.)

and in situ stress analyses is critical to fully understand geothermal systems (Davatzes and Hickman, 2010; Blake, 2013), and can have the added benefit of contributing to our understanding of regional structure and tectonics of an area. We incorporate the analysis of lithology seen in core, logs of fractures and faults, and slip indicators on small faults with the stress state to suggest a structural geological model based on Andersonian mechanics and Coulomb frictional faulting theory. This work constrains the conceptual structural and geomechanical model of the site that (1) estimates the distribution of critically stressed faults and fractures that could be conduits for fluid flow, (2) analyzes the potential connected fracture networks in the geothermal reservoir, and (3) constrains the structural setting of the MH-2 borehole in the SRP.

STUDY AREA

The SRP volcanic province (Fig. 1) is composed of a thick section of mantle-derived basalts that erupted in the axial portions of the plain over the past 6–8 m.y.; the basalt compositions are similar to mafic oceanic island basalts, like those found in the Hawaiian Island chain (Pierce and Morgan, 1992; Bonnicksen and Godchaux, 2002; Hughes et al., 2002; Pierce et al., 2002; Shervais et al., 2002). Extensive rhyolite deposits are present along the margins of the plain and have been sampled below the basalts in several deep wild-cat oil and gas drillholes. The rhyolites form by extensive fractionation of hotspot-related basalt magmas in the lower to middle crust, along with the partial assimilation of that crust (McCurry et al., 2008; McCurry and Rodgers, 2009; Knott et

al., 2016). The volcanic sequences record a complete record of volcanism from ca. 17 Ma to 200 ka in the west and volcanism as young as 2 ka in the east (Bonnicksen et al., 2008; Shervais and Hanan, 2008). The SRP is a region of high heat flow (Blackwell, 2012) sourced from emplacement of a large amount of basaltic magma in the deep to intermediate-depth crust (Nielson and Shervais, 2014).

The western SRP is a structural basin that trends ~300° and intersects the ~56°-trending eastern SRP at a high angle (Shervais and Hanan, 2008; Wood and Clemens, 2002) near the MH-2 drill site. The western SRP is bounded in part by faults that appear to be a result of a complex interaction of the SRP hotspot, Basin and Range extension beginning ca. 12 Ma (Shervais et al., 2002; Wood and Clemens, 2002), and

subsidence of the SRP. Basin-bounding, high-angle normal faults with offsets of as much as ~2750 m (Malde, 1991; Fig. 1) trend northwest-southeast. The Miocene to Pliocene paleo-Lake Idaho developed in the northwest-trending graben, which extended from the central SRP in the southeast to the Idaho-Oregon border in the northwest. Approximately 600 m of lacustrine sediments accumulated over Miocene volcanic rocks (Ruez, 2009). At present there is no geochronologic control on the age of basalts reached in the MH-2 hole. The basal sediments of Lake Idaho (Chalk Hills Formation) are 11.3–9.5 Ma (Wood and Clemens, 2002). The northeastern boundary of the basin is defined by range-front faults generally oriented 300°, as are regional faults exposed within the basin (Breckenridge et al., 2003). Small-offset faults near the MH-2 borehole (Fig. 1; Shervais et al., 2002, 2014a; Shervais, 2014) form in two clusters, one oriented ~300°, consistent with the range-front faults, and the other oriented 275° (Fig. 1). Faults on the plateau to the north are oriented more northward at 340°, and are consistent with faults mapped in the Idaho Batholith to the northeast (Breckenridge et al., 2003).

Near Mountain Home, the western SRP is underlain by a highly elongate elliptical gravity high with a 300°-trending long axis that is subparallel to the axis of the plain (Kucks, 1999; Wood and Clemens, 2002). The continuous gravity anomaly beneath the entire western SRP is interpreted as a fault-bound, intrabasin 20–30-km-wide horst delineated from seismic data that cross the plain in the area near Boise, Idaho (Wood, 1994; Wood and Clemens, 2002; Shervais and Hanan, 2008). The gravity anomaly could be the result of mafic intrusions into the crust during rifting and the extrusion of related magmas onto the surface prior to deposition in Lake Idaho (Glen and Ponce, 2002; Shervais et al., 2002). The MH-2 borehole was sited along the southwest margin of the anomaly where the gravity gradients are steepest (Shervais et al., 2013, 2014a; Shervais, 2014; Glen and Bouligand, 2014), the objective being to intercept suspected high-angle normal faults on the margins of the proposed horst block. Our exploration hypothesis was to test if the boundary of the central horst block is a zone of high fluid conductivity and convective heat flow that creates the prospect for geothermal development (Faulds et al., 2011). This paper examines the structural geology and tectonic implications of observations of the geology and in situ stresses measured in the borehole.

Three boreholes drilled near MHAFFB previous to MH-2 provide insight into the moderate-depth stratigraphy and structure across the western SRP (Fig. 1; Shervais et al., 2002;

Varriale, 2016). The Bostic-1A drillhole is a 2949 m wildcat oil and gas exploration dry hole drilled in 1974 ~35 km east of MH-2 (Arney et al., 1982, 1984). It was drilled through alternating beds of sediment and basalt, and into felsic rhyolites from ~2200 m to TD in granitic rocks (G.E. Cambell, 1974, unpublished well log; Idaho Geological Survey, http://www.idahogeology.org/Data/Oil_Gas_Scans/1972-03/1972-03_LOG_HCA_LITH_2.pdf) with a bottom hole temperature of 193 °C (thermal gradient of 66 °C/km). Arney et al. (1982, 1984) proposed that normal faults along basin-bounding faults to the northeast provided accommodation space for the volcanic deposits, but did not provide details on fault geometries due to their work with cuttings instead of whole core. The MH-1 geothermal exploration borehole was drilled on the MHAFFB in 1985 to a depth of 1342 m (Lewis and Stone, 1988). The MH-1 borehole penetrated ~580 m of lacustrine sediments with minor intercalated basalts, followed by a thick section of basalt from 580 m to TD (Lewis and Stone, 1988). The borehole was cored from 404 m to TD, where a bottom hole temperature of 95 °C was recorded. Lewis and Stone (1988) described 13 faults that dip ~45° and are partially mineralized with calcite, quartz, chlorite, pyrite, and chalcopyrite, but did not describe non-offset fractures. The Anschutz Federal No. 1 borehole is ~40 km west-southwest of MH-2, near the southwestern basin-bounding normal fault along the Owyhee Plateau (McIntyre, 1979). The borehole was logged from cuttings, so fault and fracture data are not available. The lithologies include a thick lacustrine sedimentary unit overlying rhyolite with basalt. Hydrothermal alteration concentrated in places indicates that the rocks are highly faulted and fractured in the borehole. The borehole hit basement granite near TD and may be a result of the borehole crossing a dipping normal fault and penetrating the basement in the footwall of the fault.

Borehole MH-2 was drilled on the MHAFFB between June and December 2011 (Delahunty et al. 2012, 2014; Shervais et al., 2012, 2014a). The MH-2 borehole was drilled with diamond drill wireline coring methods using a truck-mounted Atlas Copco 4002 diamond drill rig (by DOSECC Exploration Services LLC; Delahunty et al., 2014). Borehole MH-2A was abandoned at 599 m due to stuck drill rods, and a new hole, MH-2B, was drilled 7 m from the first. MH-2B was rotary drilled to 619 m, where diamond core wireline drilling recommenced. Core recovery was >96% (core recovered/cored interval). The HQ3 size core (61.1 mm diameter) was recovered from 619 m to 1144 m depth; NQ core (47.6 mm diameter) was acquired from 1144 m to TD (Fig. 2). The TD in December 2011 was 1676

m. A wireline log was acquired in January 2012, after which additional funds allowed drilling to continue to 1821 m depth. At 1745 m depth, an artesian geothermal aquifer was encountered with a temperature of at least 150 °C (Lachmar et al., 2012; Freeman, 2013; Nielson et al., 2012, 2014), indicating that the hole encountered the overpressured geothermal fluids at the base.

METHODS

We define the 540 m between 1281 m to total depth (TD) of 1821 m as the zone of interest (ZOI) in this study of MH-2. Wireline borehole geophysical logs measured properties of the rocks from the top of the ZOI to a depth of 1662 m. Wireline tools were not run deeper due to the high temperatures encountered in the base of the hole. Analyses of the wireline sonic image data and experiments to determine static and dynamic elastic properties were presented in Kessler (2014). In this study we analyze the fracture and stress data using Anderson mechanics and Coulomb frictional faulting theory to develop a structural model. (For further geologic interpretations for the area, see Kessler, 2014; Atkinson, 2015; and Varriale, 2016.)

Lithology, Fracture, and Fault Core Logging

A detailed core characterization was completed over the ZOI in MH-2 from 1280 m to the TD of 1821 m and includes descriptions of the lithology, fracture characteristics, shear failure indicators, and sampling for mechanical properties testing. We describe the lithologies and the nature of major lithologic boundaries and focus on the rock units (crystalline basalt, altered basalt, reworked basaltic sediments, basalt breccia, and hyaloclastite, a volcanic breccia formed by eruption into water or ice). Basic lithological descriptions of the core include observations of textures, groundmass, and phenocrysts. When applicable, vesicles and/or amygdules were described by distribution, size, and fill type. Alteration of basalt minerals to clay is described by the full width at half maximum in X-ray diffraction analyses, a measure of the diffracting domain size of the clays. The method is used to identify the controlling factors for alteration of volcanic glass, pyroxene, or plagioclase to clay under the particular altering environment, either weathering or hydrothermal alteration (Walker et al., 2014). Fractures were characterized by type (natural or induced), morphology (planar, curved, sealed, broken, or open), and mineral fill (calcite, quartz, zeolites, sulfides, or clay). Dip was measured with a digital protractor perpendicular to the local strike line defined by the perpendicular to the core axis. On open fractures,

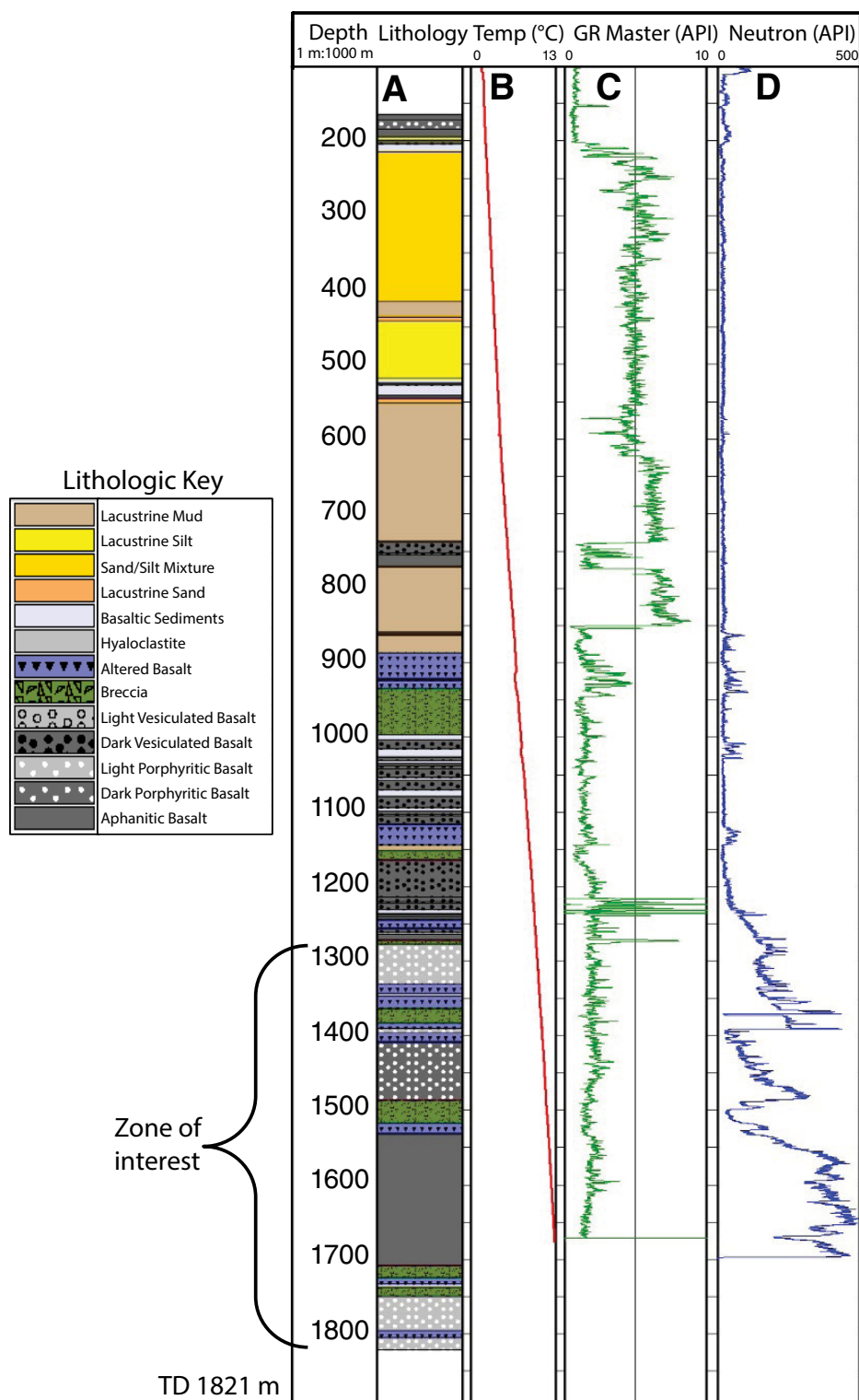


Figure 2. Lithologic log, temperature, gamma ray (GR), and neutron log for the Mountain Home 2 drillhole. Quaternary basalt flows 200 m thick overlie an ~600-m-thick sequence of lacustrine sediments. Basalt flow interbedded with thin sandstones, altered basalts, and hyaloclastites composes the lower 880 m of the borehole. Artesian flowing water with a temperature of 140 °C was encountered at 1745 m, and the zone of interest discussed here is from 1280 m to 1821 m measured depth. TD—total depth.

the fracture faces were examined for evidence of shear slip in the form of slickenlines and the rake of slickenlines was measured as the orientation of slip relative to the maximum dip direction of the fracture face. Because the borehole was essentially vertical, the angle between the core axis and any planar feature is equivalent to the dip angle. The core is unoriented, and thus fracture strike cannot be determined. Orientations can be determined where planar features can be correlated with borehole image logs.

Borehole Geophysical Data

A range of different geophysical logs was acquired in the MH-2 borehole, and the ultrasonic borehole televiewer (BHTV) is most germane to this contribution. The BHTV log (Zemanek et al., 1969) has evolved significantly from analog to digital recording technology, but the underlying operating principle remains the same. A tool centralized in the borehole emits a sequence of ultrasonic pulses centered near 1 MHz that propagate through the wellbore liquid to the borehole wall, where they are reflected back to receivers. The amplitude and the two-way transit time are extracted from the returning pulse (e.g., Schmitt et al., 1992); the former contains information on the acoustic reflectivity of the borehole wall while the latter provides a direct measure of the distance to the borehole wall. During operation, the borehole is scanned by rotating the ultrasonic beam around the borehole axis while the tool is pulled up the borehole. In an open hole the azimuth, q , of the beam with respect to magnetic north is also measured using magnetometers. The values of the reflected amplitudes and the pulse transit times are then mapped with respect to both q and depth, z , to create two unwrapped images for interpretation. (For a comprehensive review of this topic, see the compilation in Pöppelreiter et al., 2010.)

Open-hole wireline logging was carried out by the International Continental Scientific Drilling Program (<http://www.icdp-online.org>) Operational Support Group from 1144 m to 1676 m depth in early 2012. Poor borehole stability through the lacustrine sediments above this depth precluded logging higher in the borehole. Logs acquired are electrical, natural and spectral gamma, resistivity, magnetic susceptibility, temperature, dip, spontaneous potential, and sonic (Schmitt et al., 2014). Additional temperature logs were run by Pacific Process Systems, Inc. Unfortunately, in that campaign ultrasonic BHTV images could not be obtained because the temperatures in the open-hole section exceeded the available tool’s operational limits. An additional opportunity to obtain BHTV images arose after deepening of the borehole in late 2012. A

further suite of logs was obtained using higher temperature logging tools by Southwest Exploration Services LLC. A complete set of BHTV log (Advanced Logic Technologies Facsimile 40 image processing software; www.alt.lu/) generated images that were acquired downward from 1286 m measured depth (md) to 1596 m md, where the image logging tool encountered a blockage at a point where temperatures had already exceeded the higher temperature tool design. The resulting acoustic image has a nominal lateral resolution of 5 mm horizontally. The vertical resolution depended on logging speeds that were as much as 2 m/min in the lower, hotter portions of the wellbore.

Planar features appear as sinusoids on the unwrapped image logs. We used WellCad software (https://www.alt.lu/software.htm) to map the sinusoids and determine the azimuthal bearing, dip angle (δ), and aperture of the fractures. An unavoidable and long standing geometric problem is that a vertical borehole will generate a biased sampling of fractures that is a function of the core–fracture set angle (see Appendix 1). This geometric issue biases the observed count N_{δ} of the number of fractures dipping at δ to heavily weight shallowly to moderately dipping fracture planes, and depending on the fracture spacing and the length of the observation wellbore there may be fracture sets that cannot be seen. These are said to fall within the blind zone (Terzaghi, 1965), where

$$N_{90} = N_{\delta} / \cos\delta, \tag{1}$$

where N_{90} is the expected count number of fractures with dip δ . We apply a weighting factor, W , to orientation and fracture density data in order to correct the data for this bias (Priest, 1993; see Appendix 1 for details).

Mechanism of Shear Failure

The western SRP is a fault-bound basin that may be the result of complex faulting in the hanging wall of the graben (Westaway, 1990; Zhang et al., 1991; Rouby et al., 1996; Avigad et al., 1998; Boulton and Robertson, 2008; Trench, 2008). Wood (1994) (and Shervais et al., 2002) suggested the presence of intrabasinal normal faults (Fig. 2) based on seismic reflection data and the regional positive gravity anomaly. Low core recovery in the artesian flow zone at 1745 m md (<50%) suggests that there is significant large-aperture permeability at depth. We identify fault zones by defining groups or clusters of shear failure indicators in core. We used oriented fracture data from BHTV image logs and slip vector data from slickenlines to suggest a model for failure in MH-2. While the core is not

oriented, the relationship between the relative rake and the dip of the fault constrains the relative motion along the fault plane. The relative rake of slickenlines suggests a mode of failure based on the angle of dip of the fault. High-angle faults with low-rake-angle slickenlines indicate a dominant strike-slip motion on the fault, and high-angle faults with high-rake-angle slickenlines indicate dominant dip-slip motion. We relate the fracture and slickenline orientations to the possible range of stress orientations and magnitudes to suggest the mode of failure in the fault zones in MH-2.

RESULTS

MH-2 Borehole Lithology

The lithologies in MH-2 represent a history of volcanism, lacustrine deposition, hydrothermal alteration, and deposition of basaltic sediments. Crystalline basalts are often in sharp contact with hyaloclastites, hydrothermally altered basalt, and/or reworked basaltic sediments. The Mountain Home drill section consists of an upper basalt with minor interbedded sediments between 0 and 215 m md, which overlies interbedded sand, clay, minor gravel, and thin basalt layers at 215–860 m md (Fig. 2). From 850 m to 1250 m md, basalt horizons alternate with sandstone, gravels, and volcanic ash. Below 1250 m md the section consists of basalt flows, basalt hyaloclastites, and minor amounts of basaltic sands that are compact and well indurated but less dense than massive basalt (Fig. 2). We focus on the lower 540 m of core, which we call the ZOI (Figs. 2 and 3), that is marked at the top by the presence of thick aphanitic light gray basalt. The upper ~150 m of the ZOI consists of thin beds of alternating crystalline basalt with altered or reworked units. The lower part of the ZOI, from 1430 m to TD, consists of thicker packages of crystalline basalt interbedded with discrete packages of altered and reworked basalt.

We identify 42 discrete crystalline basalt flows (Fig. 3B; Table 1) that vary from 1.5 m to 19 m in thickness, 4 zones of hydrothermally altered basalt, 2 intervals of reworked basaltic sediments, and 6 zones of basaltic breccia within the lower 540 m of the MH-2 borehole (Figs. 3 and 4; Table 1). Several of the lithologic horizons are too thin to be shown in Figure 3B. These flows and sedimentary deposits fall into one of five lithologic groups (Fig. 3B). The unaltered basalt consists of two types; a light gray coarse-grained basalt and a dark gray to black, aphanitic basalt (Figs. 4A, 4B). The basalt flows exhibit varying degrees of vesicle concentration, phenocryst size, veins, and types of vein and vesicle fill (Varriale, 2016) and bulk

TABLE 1. LITHOLOGY DEPTHS DETERMINED FROM CORE

| Top depth (m) | Bottom depth (m) | Lithology |
|---------------|------------------|-----------|
| 1281.00 | 1281.92 | Lt Bst |
| 1281.92 | 1287.71 | Dk Bst |
| 1287.71 | 1289.24 | Lt Bst |
| 1289.24 | 1293.81 | Dk Bst |
| 1293.81 | 1296.86 | Lt Bst |
| 1296.86 | 1301.44 | Dk Bst |
| 1301.44 | 1305.10 | Lt Bst |
| 1305.10 | 1313.64 | Dk Bst |
| 1313.64 | 1325.84 | Lt Bst |
| 1325.84 | 1330.72 | Dk Bst |
| 1330.72 | 1342.92 | Bst Bcc |
| 1342.92 | 1347.19 | Dk Bst |
| 1347.19 | 1365.79 | Alt Bst |
| 1365.79 | 1381.35 | Bst Bcc |
| 1381.35 | 1385.92 | Bst Sed |
| 1385.92 | 1388.97 | Alt Bst |
| 1388.97 | 1394.46 | Dk Bst |
| 1394.46 | 1395.38 | Lt Bst |
| 1395.38 | 1398.43 | Dk Bst |
| 1398.43 | 1405.75 | Alt Bst |
| 1405.75 | 1408.19 | Dk Bst |
| 1408.19 | 1433.50 | Lt Bst |
| 1433.50 | 1435.94 | Dk Bst |
| 1435.94 | 1442.35 | Lt Bst |
| 1442.35 | 1451.50 | Dk Bst |
| 1451.50 | 1484.13 | Dk Bst |
| 1484.13 | 1518.60 | Bst Bcc |
| 1518.60 | 1530.19 | Alt Bst |
| 1530.19 | 1558.55 | Lt Bst |
| 1558.55 | 1560.69 | Dk Bst |
| 1560.69 | 1592.41 | Lt Bst |
| 1592.41 | 1604.91 | Dk Bst |
| 1604.91 | 1665.30 | Lt Bst |
| 1665.30 | 1708.61 | Dk Bst |
| 1708.61 | 1722.03 | Bst Bcc |
| 1722.03 | 1732.40 | Alt Bst |
| 1732.40 | 1738.50 | Bst Sed |
| 1738.50 | 1748.57 | Bst Bcc |
| 1748.57 | 1770.53 | Lt Bst |
| 1770.53 | 1776.02 | Dk Bst |
| 1776.02 | 1797.98 | Lt Bst |
| 1797.98 | 1804.69 | Bst Bcc |
| 1804.69 | 1822.68 | Dk Bst |

Note: Lt Bst—light gray basalt; Dk Bst—dark gray basalt; Bst Bcc—basaltic breccia; Alt Bst—altered basalt; Bst Sed—basaltic sediments.

densities (Table 2). Vesicles are open or filled with clay, calcite, quartz, or zeolite. Plagioclase phenocrysts vary in size from microscopic to 10 mm in length. Veins are variable in complexity and location, and are usually filled with quartz or calcite, but may also contain chlorite, pyrite, chalcopryrite, or zeolite (Walker et al., 2014; Atkinson, 2015; Varriale, 2016).

Other lithologies in the core consist of a series of altered and reworked basalt that are characterized by (1) hydrothermally altered basalt, (2) hydrothermal breccias, (3) hyaloclastite, and (4) basaltic sandstones (Figs. 4C–4F). Hydrothermally altered basalt consists of gray-green basalt with pyrite, an abundance of vuggy pore space, chlorite, clay minerals, and numerous high-gloss sheared surfaces. Hydrothermal breccias consist of angular basalt fragments

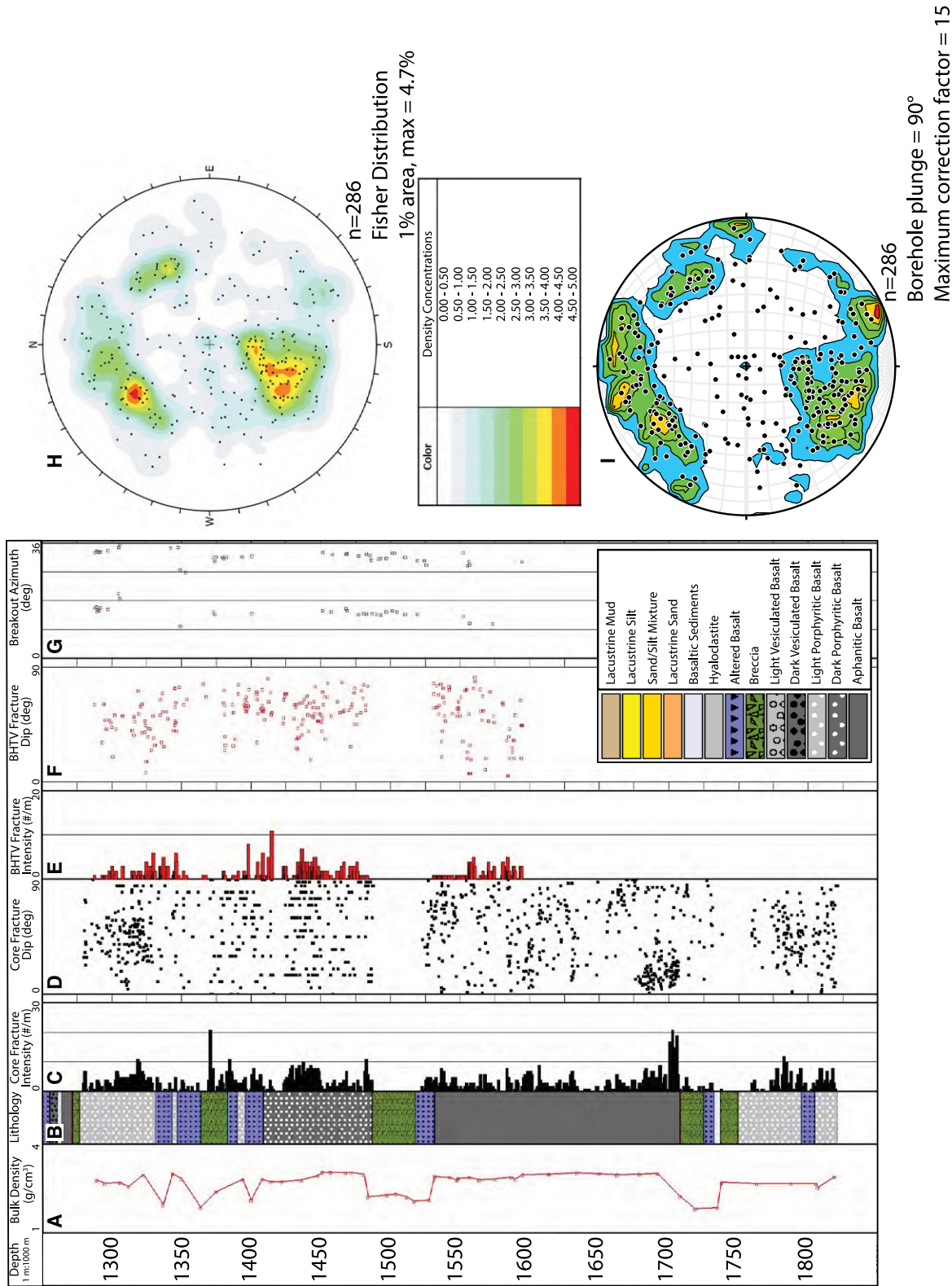


Figure 3. Detailed summary logs of the zone of interest (ZOI) region for the MH-2B borehole. (A) Bulk density data measured at the Rock Physics Lab, University of Alberta (Table 2). (B) Lithologic units defined by this study include five major basaltic and altered basalt units. The upper portion of the core consists of 1–5-m-thick basalt flows intercalated with breccia and altered basalts. The lower 60% of the core consists of thick flow units and several breccia packages. BHTV—ultrasonic borehole televiewer. (C) Fracture density (measured by number (#)/10 m interval) over the ZOI. Fracture densities are as high as 70/10 m to 10/10 m intervals, and 5 highly fractured zones broadly correlate with higher density, highly welded basalts. (D) Fracture dips and locations over the ZOI as determined from core. Because the core is nearly vertical, the core-fracture angle is approximately the dip angle. (E, F) Density and dips of natural and drilling-induced tensile fractures over the region were imaged with an acoustic image tool. (G) Azimuthal orientations for the borehole breakouts in the region measured. (H) Stereogram of poles to fractures of the natural fractures imaged in the borehole; data are contoured with Fisher statistics method. (I) Terzaghi corrected modeled data for bias due to the orientation of the borehole that would undersample steeply dipping fractures. Borehole plunge is 90°, and the maximum correction factor is 15. This stereonet was created with Stereonet version 9.8.3 (Allmendinger, <http://www.geo.cornell.edu/geology/faculty/RWA/programs/stereonet.html>), and thus the color pallet is slightly different than that in G.

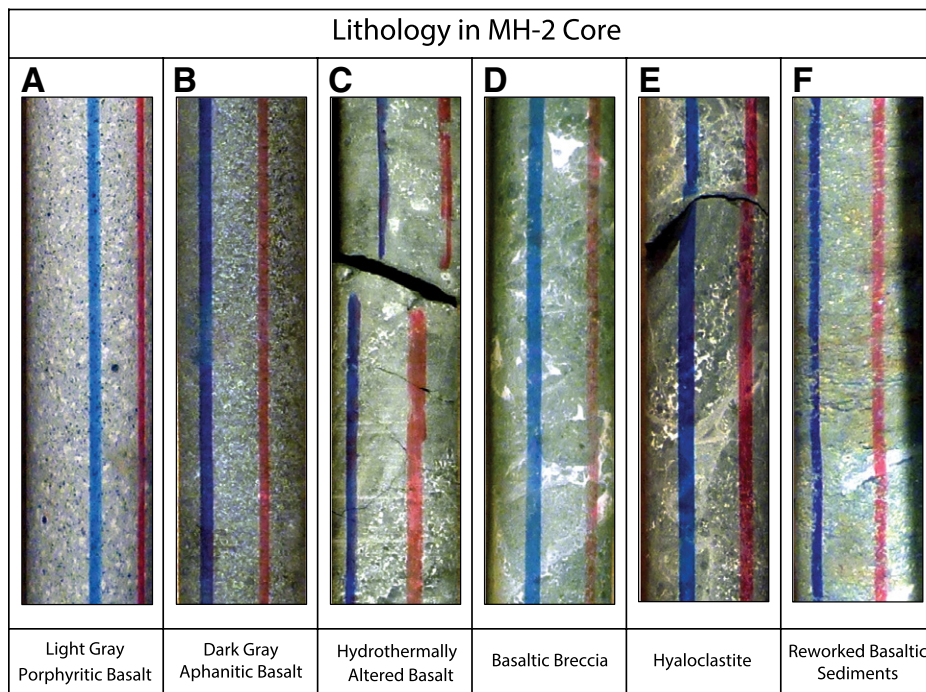


Figure 4. Examples of the lithologies observed in the lower 880 m of the MH-2 borehole. The blue and red vertical lines indicate core orientation: red is to the right to indicate that up is to the top of the page in all cases. (A) Light colored porphyritic basalt. (B) Dark gray aphanitic basalt. (C) Hydrothermally altered basalt. (D, E) Brecciated basalts that exhibit calcite veins, zones of chloritic alteration, and zones of mineralization. (F) Sedimentary facies with subhorizontal bedding in the middle of the core.

forming stockwork veins filled with calcite, quartz, chlorite, and zeolite. These breccias are interpreted as evidence for steam explosions caused by confined high-temperature hydrothermal fluids (Nielson and Shervais, 2014; Nielson et al., 2014). This interpretation is supported by fluid inclusions with equilibration temperatures in excess of 340 °C (Atkinson, 2015).

Hyaloclastites consist of glassy subangular to rounded basalt fragments, which are commonly altered to clay-rich assemblages. These may represent the flow of subaerial basalts into standing bodies of water (e.g., pillow-dammed river channels; Howard et al., 1982) or the eruption of basalt into paleo-Lake Idaho (e.g., Jenks and Bonnicksen, 1989; Godchaux et al., 1992; Bonnicksen and Godchaux, 2002). The basaltic sandstones appear to represent largely reworked hyaloclastites, formed by rapid erosion and resedimentation of hyaloclastites as lava flowed into active river channels.

Fractures and Faults

A strong association between the distribution of fractures in the MH-2 borehole and the lithological boundaries can be seen in the data (Fig. 3) where highly fractured, brittle crystalline basalt rocks are juxtaposed against ductile hyaloclastite or altered and/or reworked basalt

units. We logged a total of 1701 natural fractures and faults in the core over the ZOI between 1280 and 1821 m md (Figs. 5 and 6; Supplemental Table DR1¹). Natural fractures in the core have a range of expressions (Fig. 5), and include open, closed, sheared, and mineralized natural fractures. Simple fractures are closed to slightly open (Fig. 5A) planar fractures, typically with a thin darker coloration than the host rock, or with millimeter-thick chlorite ± calcite ± zeolite coatings (Fig. 5B). Veins in the core are relatively planar fractures with millimeter- to centimeter-thick calcite and zeolite fill (Fig. 5C), or are 1–10-cm-thick regions of veins with a brecciated texture. There are 5 regions of high natural fracture density, 20–60 m thick, that correlate between the lithologies and bulk densities in the core (Fig. 3).

Fracture and fault surfaces are commonly mineralized by calcite, amorphous silica, or fine-grained alteration products (Fig. 6). Thin faults and fracture coatings of fine-grained clay ± calcite (Figs. 6A, 6B) appear in the wall rock away from the fracture surface, indicating that

¹GSA Data Repository Item 2017171, which contains Supplemental Table DR1: Fault and fracture orientation data from core, and Supplemental Table DR2: Natural fracture orientations and apertures, is available at <http://www.geosociety.org/datarepository/2017>, or on request from editing@geosociety.org.

TABLE 2. LABORATORY DETERMINED ROCK DENSITY DATA

| Depth (m) | Density (g/cm ³) |
|-----------|------------------------------|
| 1284.6 | 2.78 |
| 1293.2 | 2.66 |
| 1305.6 | 2.68 |
| 1313.3 | 2.56 |
| 1326.1 | 2.95 |
| 1343.3 | 1.94 |
| 1350.9 | 2.99 |
| 1358.6 | 2.83 |
| 1376.3 | 1.86 |
| 1389.9 | 2.40 |
| 1412.6 | 2.80 |
| 1420.6 | 2.11 |
| 1429.3 | 2.81 |
| 1437.5 | 2.73 |
| 1444.6 | 2.73 |
| 1463.2 | 2.78 |
| 1477.5 | 2.94 |
| 1482.2 | 3.04 |
| 1488.9 | 3.05 |
| 1501.8 | 3.04 |
| 1506.6 | 3.03 |
| 1517.6 | 2.96 |
| 1521.3 | 2.21 |
| 1537.5 | 2.27 |
| 1545.2 | 2.32 |
| 1555.7 | 2.21 |
| 1562.0 | 2.08 |
| 1574.4 | 2.11 |
| 1578.8 | 2.92 |
| 1592.2 | 2.88 |
| 1599.4 | 2.85 |
| 1598.4 | 2.79 |
| 1608.4 | 2.87 |
| 1618.0 | 2.79 |
| 1632.3 | 2.83 |
| 1648.6 | 2.83 |
| 1645.7 | 2.90 |
| 1654.7 | 2.98 |
| 1679.5 | 2.99 |
| 1702.0 | 3.04 |
| 1722.0 | 3.01 |
| 1737.3 | 2.99 |
| 1757.4 | 3.01 |
| 1773.2 | 3.03 |
| 1792.2 | 2.26 |
| 1805.7 | 1.83 |
| 1824.8 | 1.88 |
| 1828.2 | 2.72 |
| 1859.3 | 2.68 |

Note: Data acquired at the Rock Physics Lab, Institute for Geophysical Research, Department of Physics, University of Alberta, Edmonton.

alteration penetrated the host rock. In other places large euhedral calcite grains (Figs. 6C, 6D) indicate the presence of relatively large open-mode fractures during mineralization. Fracture apertures are mostly between 0 and 10 mm (Fig. 7A) and the upper 300 m of the ZOI exhibit a wide range of apertures, whereas in the lower 100 m the apertures are <10 mm (Fig. 7B). Fracture dips are widely dispersed (Fig. 3D) and exhibit no orientation concentrations.

In the range from 1286 m to 1596 m md, we interpreted 286 natural fractures and 245 drilling-induced fractures imaged with the acoustic

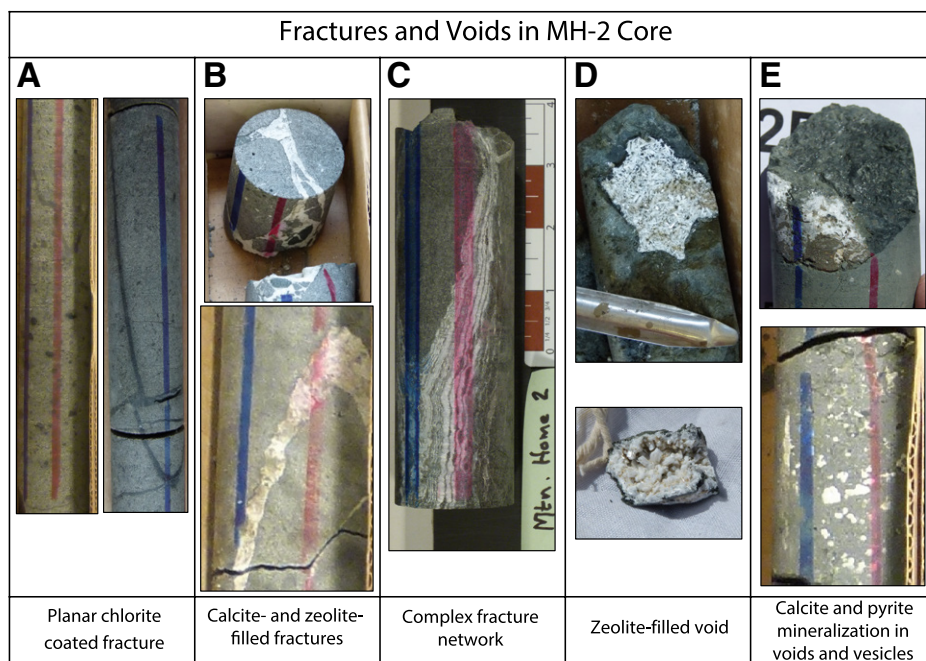


Figure 5. Examples of fractures and vesicles in the MH-2 core. (A) Relatively simple subvertical fractures are planar and typically coated by thin dark mineral coatings. (B) Simple mineralized fractures characterized by planar millimeter- to centimeter-thick calcite \pm zeolite veins. (C) Complex fractures with multiple layers, crosscutting mineralized fractures, and breccia zones. (D) Zeolite-coated fracture surfaces. (E) Calcite \pm pyrite in fractures and vesicles.

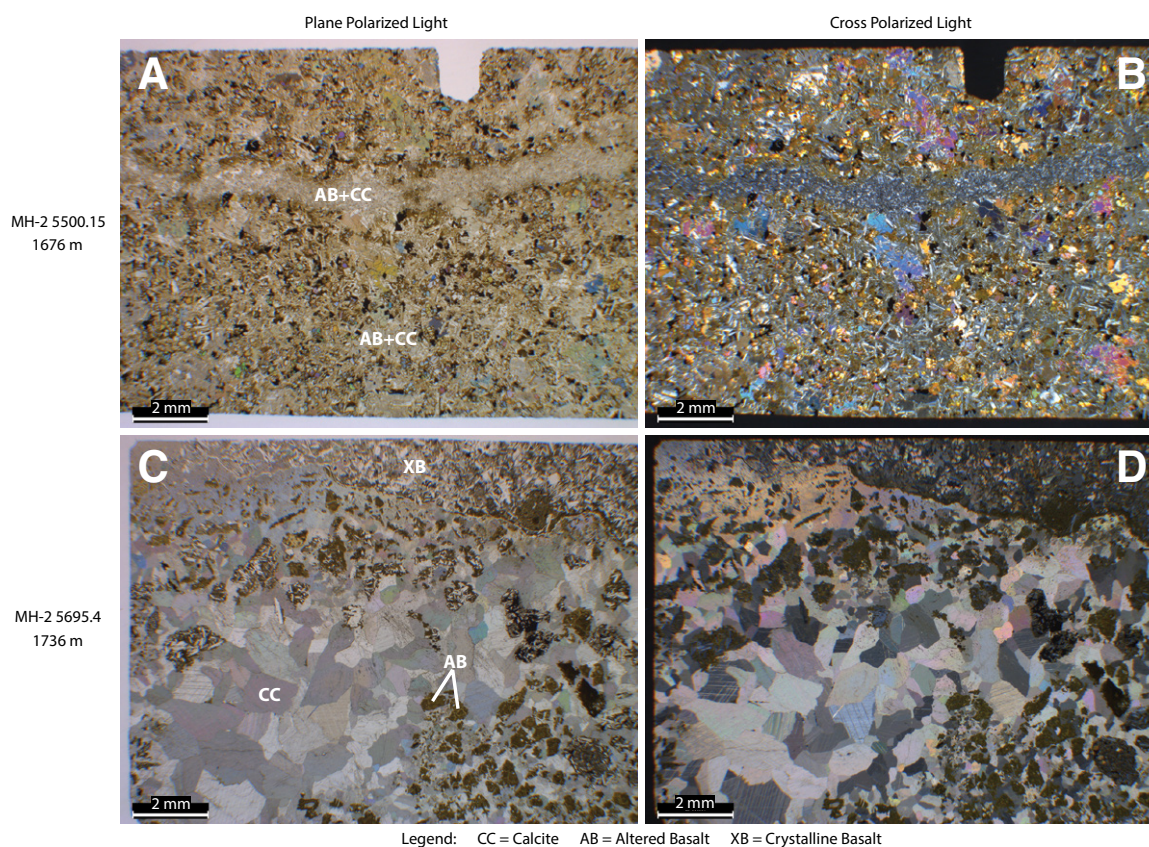


Figure 6. Photomicrographs of fracture fill from the zone of interest in the MH-2 drillhole. (A) Plane polarized light photomicrograph of fractured aphanitic basalt from 1676.4 m depth. Throughgoing fracture consists of clayey alteration material and calcite (AB + CC) with distributed zones of alteration in the basalt groundmass. (B) Cross polarized light photomicrograph of the same thin section shown in A. (C) Plane polarized light photomicrograph of brecciated basalt from 1736 m depth. The photomicrograph features abundant calcite fracture and vein filling (CC) that is superposed on altered basalt (AB) and crystalline basalt (XB). (D) Cross polarized light photomicrograph of the same thin section shown in C.

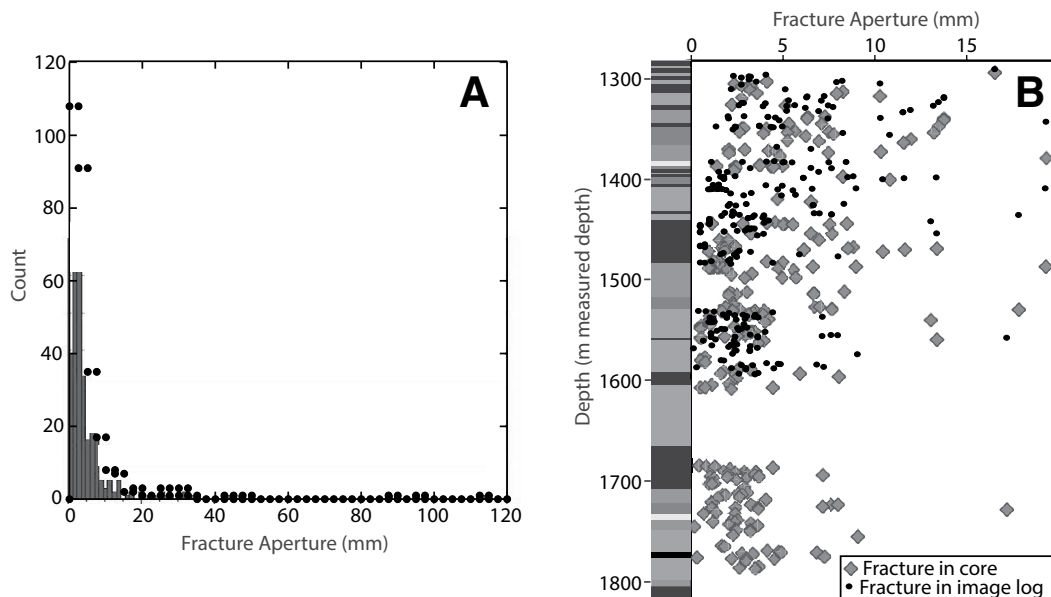


Figure 7. Aperture data for fractures measured in core and from the acoustic image log data. (A) Histogram of the fractures in the MH-2 drillhole. Most fractures have apertures <10 mm. (B) Fracture aperture as a function of depth and lithologic unit, for apertures to 20 mm. The few open fractures lie in the upper parts of the zone of interest, and there is little correlation between basalt types.

image tool (Fig. 3E; Supplemental Table DR2; Tables 3, 4A, and 4B). The BHTV results correspond well with the density and orientations of fractures logged in core (Figs. 3C–3F). Where possible we correlated the core-logged fractures with the BHTV imaged fractures and in many cases we were able to match the structures. Zones of increased fracture densities were imaged at 1286–1354, 1380–1483, and 1531–1596 m md. Fractures are concentrated in three general orientations (Fig. 3G): 290°/55°N, 060°/60°SE, and 135°/55°SW. We also observed zones of increased fracture densities below the reach of the BHTV data at 1680–1705 m md and 1750–1820 m md. The BHTV logs seem to undersample shallowly dipping fractures (cf. Figs. 3D, 3F), which may be due to difficulty in distinguishing lithologic boundaries and surfaces from fractures in the acoustically derived logs.

We applied a Terzaghi correction to the BHTV orientation data (Fig. 3I) for a 90° plunging borehole with a weighting factor of 15 (which corresponds to a core-fracture angle of ~3.8°; see Appendix 1 for details). The modeled data suggest that fractures in the rocks fall into four zones with approximate strikes and dips of 285°/65°N, 060°/65°SE, 150°/60°W, and 250°/85°N. Applying the same weighting factor to the fracture densities measured in core would result in fracture densities that are increased by 30%–50% above those shown in Figures 3C and 3E. Many of the fractures that might remain undersampled by the core and BHTV likely are cooling fractures in the basalts common throughout the area (Shervais et al., 2002).

We logged 166 faults in the core. Faults are recognized by the presence of slickenlines and

high gloss surfaces (Fig. 8). We observed structural slickenlines and mineral lineations in the core (Figs. 8C, 8D). Structural slickenlines on the fault surfaces are carved grooves in the fault faces, whereas mineral lineations are those that are a result of smearing of mineral grains during slip events. At the core scale, the fault zones are associated with zones of altered basalt, reworked basaltic sediments, basaltic breccias, and hyaloclastites. The faults are clustered around the ductile units, but faults are also present in the brittle units directly above and beneath the ductile caprock and brittle reservoir unit combination.

The fault planes cluster in four horizons of fault concentrations (Fig. 9) that broadly correspond to the location of the stiffer units as defined by the bulk density (Fig. 3C; Table 2) as well as rock mechanics data (Kessler, 2014). Fault dips and slip rake angles vary randomly with depth (Fig. 9). The mean fault dip is 45.9° with a wide dispersion (Fig. 10A) and the dips are bimodally concentrated at ~30° and at 50°–60° (Fig. 10A). The slip vectors are strongly oblique; most of the rake values are between 0° and 60° (Fig. 10A) with a mean of 35.6° skewed to the shallow values (Fig. 10A). No correlations exist between the dip of the fault and the rake of the slip vectors (Fig. 10B), although there is a weak clustering of shallow rakes for fault dips between ~30° and 65° (Fig. 10B).

We cannot determine the amount of offset along the faults in a single borehole, but the distinct change in lithology from weak, compliant units to strong, stiff units that we interpret as a potential cap rock–reservoir structural and stratigraphic relationship and the clustering of

shear slip surfaces near those contacts suggests a large enough amount of offset in the fault zones to juxtapose the lithologic units and create a structural trap for hydrothermal fluids. The wide distribution of slip angles (Fig. 10) on the shear surfaces indicates oblique failure in the fault zones and suggests a complex fault zone.

Stress Orientations

Principal horizontal stress axes orientations are identified through interpretation of borehole breakouts and drilling-induced tensile fractures in ultrasonic acoustic borehole viewer data (Fig. 11). We determined the orientations of 196 borehole breakouts (Fig. 12; Table 4A) and 245 drilling-induced tensile fractures (Table 4B). The borehole breakout fractures are centimeter-scale open fractures that are subvertical and 180° apart on the borehole wall (Fig. 12). The drilling-induced fractures are thin, irregularly shaped, and discontinuous. The breakout orientations are consistent over the entire depth of the ZOI (Figs. 12A and 13). The region between 1280 and 1401 m md exhibits a mean breakout orientation of 316.8°, with a standard deviation of 34° (Fig. 12B); the region between 1401 and 1450 m md is devoid of breakouts, and from 1450 m md to TD the mean breakout value is 315.4° ± 13.76°, with a slight drift to a more west-northwest orientation at depth (Figs. 12C and 13). These data are consistent over the sampled interval of the ZOI and indicate a consistent maximum principal horizontal stress (S_H) direction of 045°–047° (Fig. 12A).

The maximum principal horizontal stress oriented at ~047° is nearly perpendicular to the

TABLE 3. NATURAL FRACTURES LOGGED FROM THE BHTV DATA

| Unit | Depth (m) | Azimuth (°) | Strike (°) | Dip (°) | Aperture (mm) | Type |
|------|-----------|-------------|------------|---------|---------------|------|
| 9 | 1287.8 | 222.54 | 132.54 | 60.62 | 16.53 | 1 |
| 9 | 1293.4 | 350.94 | 260.94 | 30.96 | 4.08 | 2 |
| 9 | 1294.6 | 172.91 | 82.91 | 60.95 | 2.31 | 2 |
| 9 | 1295.1 | 66.17 | 336.17 | 48.44 | 3.16 | 2 |
| 9 | 1295.4 | 260.74 | 170.74 | 48.44 | 3.24 | 2 |
| 9 | 1296.3 | 44.90 | 314.90 | 41.61 | 2.74 | 2 |
| 9 | 1298.3 | 321.79 | 231.79 | 48.44 | 3.16 | 3 |
| 9 | 1299.6 | 51.60 | 321.60 | 46.56 | 8.23 | 3 |
| 9 | 1300.4 | 18.91 | 288.91 | 43.11 | 3.56 | 2 |
| 9 | 1300.8 | 354.88 | 264.88 | 19.80 | 7.92 | 2 |
| 9 | 1302.3 | 354.88 | 264.88 | 52.35 | 10.29 | 1 |
| 9 | 1303.4 | 350.94 | 260.94 | 41.61 | 2.74 | 2 |
| 9 | 1307.8 | 194.57 | 104.57 | 51.83 | 2.19 | 3 |
| 9 | 1308.1 | 29.93 | 299.93 | 51.83 | 5.13 | 3 |
| 9 | 1314.9 | 25.60 | 295.60 | 40.43 | 7.25 | 2 |
| 9 | 1315.2 | 35.45 | 305.45 | 40.43 | 6.32 | 2 |
| 9 | 1316.0 | 14.18 | 284.18 | 36.65 | 13.77 | 1 |
| 9 | 1316.3 | 148.49 | 58.49 | 51.30 | 6.29 | 2 |
| 9 | 1316.9 | 356.06 | 266.06 | 47.50 | 13.77 | 1 |
| 9 | 1319.3 | 177.24 | 87.24 | 71.63 | 5.31 | 1 |
| 9 | 1319.5 | 353.70 | 263.70 | 53.60 | 7.10 | 1 |
| 9 | 1321.0 | 224.51 | 134.51 | 59.43 | 13.47 | 1 |
| 9 | 1321.9 | 29.93 | 299.93 | 38.77 | 2.76 | 2 |
| 9 | 1321.9 | 27.18 | 297.18 | 38.77 | 2.86 | 2 |
| 9 | 1322.1 | 296.59 | 206.59 | 61.27 | 4.05 | 1 |
| 9 | 1324.1 | 25.60 | 295.60 | 47.83 | 5.65 | 2 |
| 9 | 1324.3 | 24.42 | 294.42 | 44.54 | 2.61 | 2 |
| 9 | 1324.4 | 21.27 | 291.27 | 39.21 | 7.47 | 1 |
| 9 | 1324.7 | 14.57 | 284.57 | 7.51 | 13.19 | 1 |
| 9 | 1324.9 | 100.44 | 10.44 | 16.07 | 5.21 | 1 |
| 9 | 1325.1 | 338.34 | 248.34 | 16.07 | 3.92 | 2 |
| 9 | 1325.9 | 5.91 | 275.91 | 35.76 | 7.73 | 1 |
| 9 | 1326.7 | 106.35 | 16.35 | 42.36 | 6.22 | 2 |
| 9 | 1327.6 | 293.83 | 203.83 | 41.59 | 47.57 | 1 |
| 9 | 1328.8 | 16.94 | 286.94 | 25.06 | 11.94 | 1 |
| 9 | 1328.9 | 13.00 | 283.00 | 25.06 | 23.89 | 1 |
| 9 | 1329.7 | 180.00 | 90.00 | 51.83 | 5.21 | 2 |
| 9 | 1330.0 | 356.46 | 266.46 | 34.40 | 6.95 | 1 |
| 9 | 1330.1 | 11.82 | 281.82 | 34.40 | 6.95 | 1 |
| 9 | 1331.1 | 326.91 | 236.91 | 28.89 | 11.54 | 1 |
| 9 | 1331.3 | 3.54 | 273.54 | 28.89 | 11.54 | 1 |
| 9 | 1335.2 | 88.23 | 358.23 | 52.59 | 2.89 | 2 |
| 9 | 1335.3 | 61.84 | 331.84 | 64.91 | 2.02 | 2 |
| 9 | 1335.9 | 354.88 | 264.88 | 30.99 | 4.19 | 2 |
| 9 | 1336.0 | 356.46 | 266.46 | 30.99 | 4.19 | 2 |
| 9 | 1336.5 | 231.60 | 141.60 | 69.59 | 4.60 | 3 |
| 9 | 1336.8 | 192.60 | 102.60 | 55.21 | 10.31 | 3 |
| 9 | 1337.4 | 352.12 | 262.12 | 27.83 | 7.45 | 4 |
| 9 | 1337.4 | 20.09 | 290.09 | 27.83 | 2.05 | 4 |
| 9 | 1339.3 | 14.57 | 284.57 | 55.23 | 4.80 | 1 |
| 9 | 1340.7 | 10.24 | 280.24 | 49.62 | 19.32 | 1 |
| 9 | 1344.7 | 354.88 | 264.88 | 40.39 | 3.72 | 2 |
| 9 | 1345.3 | 146.52 | 56.52 | 44.54 | 3.72 | 2 |
| 9 | 1345.5 | 250.90 | 160.90 | 73.20 | 4.97 | 1 |
| 9 | 1345.6 | 243.81 | 153.81 | 73.86 | 1.36 | 2 |
| 9 | 1345.7 | 153.61 | 63.61 | 47.83 | 2.40 | 2 |
| 9 | 1345.8 | 222.93 | 132.93 | 58.88 | 4.35 | 2 |
| 9 | 1346.2 | 339.91 | 249.91 | 46.56 | 2.43 | 3 |
| 9 | 1346.4 | 271.38 | 181.38 | 62.34 | 4.48 | 3 |
| 9 | 1346.7 | 308.01 | 218.01 | 40.03 | 113.01 | 1 |
| 9 | 1348.6 | 313.52 | 223.52 | 74.28 | 2.28 | 4 |
| 9 | 1352.1 | 174.49 | 84.49 | 60.62 | 8.26 | 4 |
| 9 | 1354.0 | 195.36 | 105.36 | 64.66 | 10.81 | 4 |
| 8 | 1366.0 | 196.54 | 106.54 | 76.75 | 4.67 | 4 |
| 8 | 1368.0 | 196.54 | 106.54 | 67.17 | 6.53 | 4 |
| 7 | 1380.4 | 124.46 | 34.46 | 61.89 | 4.54 | 3 |
| 7 | 1380.9 | 163.06 | 73.06 | 71.84 | 4.11 | 2 |
| 7 | 1381.2 | 313.13 | 223.13 | 70.55 | 2.80 | 4 |
| 7 | 1381.2 | 29.93 | 299.93 | 25.06 | 1.11 | 2 |
| 7 | 1381.3 | 216.24 | 126.24 | 59.95 | 8.44 | 2 |
| 7 | 1381.4 | 246.56 | 156.56 | 52.87 | 5.08 | 2 |
| 7 | 1381.6 | 245.38 | 155.38 | 35.72 | 7.50 | 2 |

(continued)

TABLE 3. NATURAL FRACTURES LOGGED FROM THE BHTV DATA (continued)

| Unit | Depth (m) | Azimuth (°) | Strike (°) | Dip (°) | Aperture (mm) | Type |
|------|-----------|-------------|------------|---------|---------------|------|
| 7 | 1381.7 | 22.84 | 292.84 | 35.76 | 5.00 | 2 |
| 7 | 1381.7 | 33.87 | 303.87 | 28.90 | 5.50 | 2 |
| 7 | 1387.2 | 154.79 | 64.79 | 60.62 | 6.53 | 1 |
| 7 | 1387.5 | 117.37 | 27.37 | 28.40 | 3.22 | 2 |
| 7 | 1387.6 | 27.18 | 297.18 | 54.54 | 7.65 | 1 |
| 7 | 1389.0 | 227.26 | 137.26 | 33.88 | 30.91 | 1 |
| 7 | 1391.2 | 11.82 | 281.82 | 65.40 | 1.52 | 4 |
| 7 | 1391.2 | 286.74 | 196.74 | 69.43 | 6.95 | 1 |
| 7 | 1391.3 | 267.44 | 177.44 | 76.31 | 1.97 | 3 |
| 7 | 1395.5 | 16.15 | 286.15 | 60.62 | 2.40 | 2 |
| 7 | 1395.7 | 34.27 | 304.27 | 58.12 | 8.83 | 2 |
| 7 | 1396.1 | 344.64 | 254.64 | 63.89 | 1.61 | 2 |
| 7 | 1396.3 | 26.00 | 296.00 | 59.59 | 1.79 | 2 |
| 7 | 1396.4 | 37.02 | 307.02 | 55.66 | 95.43 | 1 |
| 7 | 1396.6 | 25.60 | 295.60 | 66.75 | 8.53 | 1 |
| 7 | 1396.8 | 69.32 | 339.32 | 59.59 | 13.35 | 1 |
| 7 | 1397.2 | 31.51 | 301.51 | 62.34 | 6.12 | 4 |
| 7 | 1397.3 | 115.01 | 25.01 | 55.22 | 6.12 | 4 |
| 7 | 1397.6 | 37.02 | 307.02 | 57.54 | 11.60 | 1 |
| 7 | 1398.2 | 237.11 | 147.11 | 59.59 | 1.79 | 4 |
| 7 | 1398.3 | 124.46 | 34.46 | 59.59 | 1.79 | 4 |
| 7 | 1398.4 | 113.44 | 23.44 | 59.59 | 1.79 | 4 |
| 7 | 1398.4 | 215.05 | 125.05 | 59.59 | 0.97 | 4 |
| 7 | 1398.7 | 33.48 | 303.48 | 72.49 | 10.43 | 1 |
| 7 | 1404.1 | 322.98 | 232.98 | 70.85 | 1.50 | 4 |
| 7 | 1404.3 | 298.16 | 208.16 | 69.08 | 1.50 | 4 |
| 7 | 1404.4 | 298.16 | 208.16 | 64.66 | 1.20 | 4 |
| 7 | 1404.8 | 281.23 | 191.23 | 30.94 | 4.08 | 4 |
| 7 | 1405.2 | 39.39 | 309.39 | 53.83 | 4.97 | 4 |
| 7 | 1407.4 | 9.06 | 279.06 | 57.34 | 88.73 | 1 |
| 7 | 1407.9 | 235.54 | 145.54 | 57.52 | 8.98 | 3 |
| 7 | 1407.9 | 37.81 | 307.81 | 72.36 | 19.28 | 1 |
| 7 | 1408.2 | 24.42 | 294.42 | 59.94 | 6.60 | 1 |
| 7 | 1408.3 | 139.82 | 49.82 | 55.22 | 1.10 | 4 |
| 7 | 1408.3 | 133.92 | 43.92 | 55.22 | 1.20 | 4 |
| 7 | 1408.4 | 143.76 | 53.76 | 55.22 | 1.50 | 4 |
| 7 | 1408.5 | 142.58 | 52.58 | 55.22 | 1.40 | 4 |
| 7 | 1408.5 | 124.46 | 34.46 | 55.22 | 1.70 | 4 |
| 7 | 1408.6 | 124.46 | 34.46 | 55.22 | 1.10 | 4 |
| 7 | 1408.7 | 142.58 | 52.58 | 55.22 | 1.06 | 4 |
| 7 | 1408.8 | 142.58 | 52.58 | 55.22 | 0.95 | 4 |
| 7 | 1409.0 | 128.40 | 38.40 | 55.88 | 4.72 | 4 |
| 7 | 1409.5 | 148.49 | 58.49 | 57.34 | 1.91 | 4 |
| 7 | 1409.9 | 126.04 | 36.04 | 48.75 | 5.55 | 4 |
| 7 | 1412.5 | 182.76 | 92.76 | 81.26 | 3.28 | 4 |
| 7 | 1412.9 | 7.97 | 277.97 | 63.06 | 2.16 | 4 |
| 7 | 1414.3 | 26.39 | 296.39 | 70.24 | 5.69 | 4 |
| 7 | 1414.8 | 139.82 | 49.82 | 52.85 | 2.87 | 4 |
| 7 | 1415.0 | 25.60 | 295.60 | 54.30 | 4.92 | 4 |
| 7 | 1415.1 | 17.33 | 287.33 | 54.30 | 21.73 | 4 |
| 7 | 1423.4 | 31.12 | 301.12 | 45.90 | 8.32 | 1 |
| 7 | 1423.5 | 1.97 | 271.97 | 64.41 | 2.11 | 4 |
| 7 | 1423.7 | 4.73 | 274.73 | 50.19 | 3.01 | 2 |
| 7 | 1424.5 | 350.94 | 260.94 | 66.75 | 6.65 | 1 |
| 7 | 1424.7 | 1.97 | 271.97 | 69.43 | 6.65 | 4 |
| 7 | 1424.8 | 7.48 | 277.48 | 66.75 | 6.65 | 1 |
| 7 | 1425.1 | 11.82 | 281.82 | 69.43 | 2.44 | 4 |
| 7 | 1425.4 | 16.15 | 286.15 | 69.43 | 2.02 | 4 |
| 7 | 1431.0 | 144.16 | 54.16 | 49.90 | 2.28 | 2 |
| 7 | 1431.5 | 21.66 | 291.66 | 60.62 | 2.28 | 2 |
| 6 | 1432.6 | 18.91 | 288.91 | 58.67 | 1.84 | 2 |
| 6 | 1432.7 | 33.87 | 303.87 | 60.62 | 2.34 | 4 |
| 6 | 1432.9 | 355.27 | 265.27 | 26.75 | 6.70 | 4 |
| 6 | 1433.0 | 285.95 | 195.95 | 33.90 | 6.99 | 4 |
| 6 | 1433.8 | 3.54 | 273.54 | 25.64 | 7.65 | 4 |
| 6 | 1434.2 | 317.46 | 227.46 | 42.36 | 7.65 | 4 |
| 6 | 1434.3 | 338.34 | 248.34 | 34.84 | 31.56 | 2 |
| 6 | 1434.6 | 28.36 | 298.36 | 71.43 | 2.64 | 4 |
| 6 | 1434.6 | 16.15 | 286.15 | 34.84 | 17.83 | 4 |
| 6 | 1435.0 | 49.23 | 319.23 | 61.89 | 3.45 | 4 |
| 6 | 1435.0 | 184.33 | 94.33 | 61.89 | 3.97 | 4 |
| 6 | 1435.1 | 189.85 | 99.85 | 61.89 | 2.24 | 4 |

(continued)

TABLE 3. NATURAL FRACTURES LOGGED FROM THE BHTV DATA (continued)

| Unit | Depth (m) | Azimuth (°) | Strike (°) | Dip (°) | Aperture (mm) | Type |
|------|-----------|-------------|------------|---------|---------------|------|
| 6 | 1435.2 | 14.57 | 284.57 | 61.89 | 2.24 | 4 |
| 6 | 1435.6 | 354.09 | 264.09 | 61.89 | 1.67 | 4 |
| 6 | 1436.7 | 15.75 | 285.75 | 45.23 | 3.35 | 4 |
| 6 | 1436.8 | 21.66 | 291.66 | 37.08 | 26.78 | 2 |
| 6 | 1437.3 | 170.15 | 80.15 | 62.34 | 3.91 | 2 |
| 6 | 1437.7 | 57.90 | 327.90 | 49.04 | 3.12 | 2 |
| 6 | 1437.9 | 225.69 | 135.69 | 49.04 | 3.12 | 2 |
| 6 | 1438.6 | 3.15 | 273.15 | 64.66 | 1.00 | 2 |
| 6 | 1440.3 | 165.82 | 75.82 | 59.41 | 4.22 | 2 |
| 6 | 1440.6 | 338.73 | 248.73 | 67.58 | 1.00 | 4 |
| 6 | 1441.0 | 64.99 | 334.99 | 52.84 | 13.05 | 1 |
| 6 | 1441.3 | 75.62 | 345.62 | 40.03 | 1.00 | 2 |
| 6 | 1442.4 | 44.90 | 314.90 | 61.74 | 3.99 | 1 |
| 6 | 1443.0 | 55.93 | 325.93 | 17.33 | 1.00 | 2 |
| 6 | 1444.0 | 44.90 | 314.90 | 51.83 | 1.00 | 4 |
| 6 | 1444.6 | 153.61 | 63.61 | 58.50 | 0.50 | 4 |
| 6 | 1445.0 | 159.12 | 69.12 | 50.76 | 2.32 | 2 |
| 6 | 1445.4 | 129.98 | 39.98 | 58.50 | 0.50 | 4 |
| 6 | 1445.7 | 148.10 | 58.10 | 63.06 | 0.50 | 4 |
| 6 | 1445.9 | 159.12 | 69.12 | 53.60 | 0.50 | 4 |
| 6 | 1446.3 | 120.13 | 30.13 | 74.77 | 0.50 | 4 |
| 6 | 1448.0 | 246.56 | 156.56 | 47.83 | 3.10 | 4 |
| 6 | 1448.1 | 13.00 | 283.00 | 47.83 | 3.30 | 4 |
| 6 | 1448.2 | 152.04 | 62.04 | 58.12 | 3.45 | 4 |
| 6 | 1448.4 | 1.58 | 271.58 | 47.83 | 3.20 | 4 |
| 6 | 1448.7 | 350.94 | 260.94 | 47.83 | 3.20 | 2 |
| 6 | 1449.2 | 358.03 | 268.03 | 53.83 | 3.20 | 2 |
| 6 | 1450.4 | 39.39 | 309.39 | 52.84 | 2.95 | 2 |
| 6 | 1450.7 | 172.91 | 82.91 | 46.56 | 2.52 | 2 |
| 6 | 1451.2 | 185.51 | 95.51 | 40.03 | 1.80 | 4 |
| 6 | 1451.4 | 13.39 | 283.39 | 49.62 | 1.80 | 4 |
| 6 | 1451.5 | 165.03 | 75.03 | 70.70 | 0.50 | 4 |
| 6 | 1451.7 | 183.15 | 93.15 | 70.70 | 0.50 | 4 |
| 6 | 1452.2 | 84.29 | 354.29 | 60.62 | 0.50 | 4 |
| 6 | 1453.2 | 169.76 | 79.76 | 66.54 | 13.37 | 1 |
| 6 | 1453.6 | 3.54 | 273.54 | 33.93 | 3.95 | 2 |
| 6 | 1455.2 | 115.40 | 25.40 | 77.37 | 3.62 | 4 |
| 6 | 1455.4 | 144.95 | 54.95 | 66.75 | 31.75 | 1 |
| 6 | 1457.7 | 160.70 | 70.70 | 51.83 | 34.10 | 4 |
| 6 | 1462.1 | 148.10 | 58.10 | 62.79 | 25.23 | 1 |
| 6 | 1464.1 | 249.32 | 159.32 | 54.32 | 0.75 | 4 |
| 6 | 1465.6 | 339.52 | 249.52 | 78.29 | 0.50 | 2 |
| 6 | 1466.2 | 157.55 | 67.55 | 55.21 | 0.50 | 4 |
| 6 | 1467.1 | 178.42 | 88.42 | 56.10 | 0.75 | 4 |
| 6 | 1470.5 | 35.45 | 305.45 | 56.52 | 2.63 | 2 |
| 6 | 1471.7 | 193.79 | 103.79 | 27.83 | 3.24 | 2 |
| 6 | 1472.1 | 236.72 | 146.72 | 58.87 | 2.52 | 2 |
| 6 | 1472.8 | 51.99 | 321.99 | 61.27 | 1.76 | 2 |
| 6 | 1474.1 | 131.55 | 41.55 | 70.08 | 1.62 | 1 |
| 6 | 1474.3 | 243.81 | 153.81 | 45.55 | 5.90 | 1 |
| 6 | 1474.4 | 163.46 | 73.46 | 73.76 | 2.36 | 1 |
| 6 | 1476.3 | 202.06 | 112.06 | 52.61 | 8.00 | 1 |
| 6 | 1476.9 | 267.44 | 177.44 | 45.24 | 2.49 | 2 |
| 6 | 1479.2 | 9.06 | 279.06 | 54.30 | 2.14 | 2 |
| 6 | 1479.7 | 204.03 | 114.03 | 71.97 | 26.37 | 1 |
| 6 | 1480.6 | 176.85 | 86.85 | 65.40 | 2.03 | 2 |
| 6 | 1481.1 | 134.70 | 44.70 | 76.46 | 1.11 | 4 |
| 6 | 1482.5 | 241.05 | 151.05 | 56.52 | 0.50 | 4 |
| 6 | 1482.7 | 263.50 | 173.50 | 58.12 | 4.45 | 4 |
| 6 | 1482.7 | 271.38 | 181.38 | 60.28 | 0.75 | 4 |
| 6 | 1483.8 | 167.79 | 77.79 | 75.05 | 2.17 | 1 |
| 4 | 1531.2 | 324.55 | 234.55 | 58.12 | 0.40 | 2 |
| 4 | 1531.5 | 336.76 | 246.76 | 77.21 | 0.81 | 4 |
| 4 | 1531.8 | 321.79 | 231.79 | 69.08 | 1.26 | 2 |
| 4 | 1532.6 | 334.00 | 244.00 | 58.12 | 4.45 | 1 |
| 4 | 1533.3 | 67.35 | 337.35 | 75.74 | 2.07 | 2 |
| 4 | 1533.9 | 42.54 | 312.54 | 58.88 | 43.40 | 1 |
| 4 | 1534.7 | 334.00 | 244.00 | 68.45 | 1.75 | 4 |
| 4 | 1535.0 | 331.25 | 241.25 | 68.45 | 3.50 | 2 |
| 4 | 1535.2 | 77.20 | 347.20 | 53.35 | 2.84 | 4 |
| 4 | 1535.4 | 335.58 | 245.58 | 59.95 | 2.38 | 2 |
| 4 | 1536.3 | 336.76 | 246.76 | 76.68 | 1.94 | 4 |

(continued)

TABLE 3. NATURAL FRACTURES LOGGED FROM THE BHTV DATA (continued)

| Unit | Depth (m) | Azimuth (°) | Strike (°) | Dip (°) | Aperture (mm) | Type |
|------|-----------|-------------|------------|---------|---------------|------|
| 4 | 1536.4 | 331.64 | 241.64 | 76.68 | 3.04 | 4 |
| 4 | 1537.0 | 183.15 | 93.15 | 19.80 | 3.45 | 2 |
| 4 | 1537.1 | 241.05 | 151.05 | 31.96 | 7.15 | 4 |
| 4 | 1537.7 | 126.04 | 36.04 | 40.03 | 3.65 | 2 |
| 4 | 1537.8 | 124.46 | 34.46 | 40.03 | 3.65 | 2 |
| 4 | 1538.0 | 349.37 | 259.37 | 73.65 | 1.03 | 2 |
| 4 | 1538.2 | 40.96 | 310.96 | 66.43 | 1.95 | 2 |
| 4 | 1538.9 | 225.69 | 135.69 | 62.19 | 1.21 | 2 |
| 4 | 1539.2 | 235.54 | 145.54 | 51.83 | 2.94 | 2 |
| 4 | 1540.0 | 44.90 | 314.90 | 47.82 | 2.46 | 2 |
| 4 | 1542.1 | 239.87 | 149.87 | 74.57 | 1.27 | 4 |
| 4 | 1542.3 | 185.51 | 95.51 | 74.57 | 0.97 | 4 |
| 4 | 1542.6 | 210.72 | 120.72 | 72.23 | 1.12 | 4 |
| 4 | 1544.6 | 248.93 | 158.93 | 53.83 | 2.88 | 2 |
| 4 | 1548.0 | 237.11 | 147.11 | 51.83 | 3.05 | 2 |
| 4 | 1548.5 | 248.14 | 158.14 | 57.74 | 2.54 | 2 |
| 4 | 1549.2 | 232.78 | 142.78 | 55.66 | 2.75 | 2 |
| 4 | 1549.3 | 254.84 | 164.84 | 63.06 | 1.66 | 2 |
| 4 | 1549.5 | 246.96 | 156.96 | 58.50 | 1.85 | 2 |
| 4 | 1550.5 | 143.76 | 53.76 | 51.83 | 2.61 | 2 |
| 4 | 1551.2 | 138.25 | 48.25 | 66.54 | 1.41 | 2 |
| 4 | 1552.2 | 177.24 | 87.24 | 32.01 | 4.04 | 2 |
| 4 | 1553.8 | 198.12 | 108.12 | 72.03 | 1.09 | 4 |
| 4 | 1553.9 | 114.62 | 24.62 | 72.03 | 1.10 | 4 |
| 4 | 1555.1 | 183.94 | 93.94 | 72.54 | 3.22 | 1 |
| 4 | 1555.4 | 133.92 | 43.92 | 23.37 | 7.62 | 1 |
| 4 | 1555.6 | 156.37 | 66.37 | 18.57 | 7.98 | 1 |
| 4 | 1556.5 | 167.79 | 77.79 | 53.35 | 7.14 | 1 |
| 4 | 1556.8 | 226.08 | 136.08 | 6.84 | 3.64 | 2 |
| 4 | 1557.3 | 92.17 | 2.17 | 6.84 | 2.40 | 2 |
| 4 | 1557.4 | 88.62 | 358.62 | 28.90 | 1.10 | 2 |
| 4 | 1557.6 | 306.43 | 216.43 | 6.84 | 1.10 | 2 |
| 4 | 1557.9 | 131.16 | 41.16 | 6.84 | 3.64 | 2 |
| 4 | 1558.2 | 89.80 | 359.80 | 17.33 | 17.18 | 1 |
| 4 | 1560.0 | 271.38 | 181.38 | 73.76 | 1.33 | 2 |
| 4 | 1561.0 | 264.68 | 174.68 | 81.95 | 2.34 | 1 |
| 4 | 1561.1 | 200.88 | 110.88 | 79.03 | 0.67 | 4 |
| 4 | 1565.0 | 159.12 | 69.12 | 72.73 | 2.50 | 1 |
| 4 | 1565.3 | 218.99 | 128.99 | 55.66 | 2.17 | 2 |
| 4 | 1566.0 | 83.89 | 353.89 | 71.14 | 1.14 | 4 |
| 4 | 1566.0 | 219.78 | 129.78 | 48.44 | 2.35 | 2 |
| 4 | 1566.7 | 200.88 | 110.88 | 67.48 | 3.23 | 1 |
| 4 | 1567.4 | 188.27 | 98.27 | 55.88 | 2.05 | 1 |
| 4 | 1568.4 | 210.33 | 120.33 | 9.56 | 3.61 | 4 |
| 4 | 1569.0 | 83.89 | 353.89 | 18.57 | 0.14 | 4 |
| 4 | 1570.7 | 81.14 | 351.14 | 47.83 | 3.20 | 2 |
| 4 | 1570.8 | 78.38 | 348.38 | 47.83 | 2.38 | 2 |
| 4 | 1571.1 | 32.69 | 302.69 | 47.83 | 2.46 | 2 |
| 4 | 1571.7 | 150.46 | 60.46 | 70.70 | 3.20 | 1 |
| 4 | 1574.4 | 18.51 | 288.51 | 51.83 | 2.26 | 4 |
| 4 | 1574.8 | 36.63 | 306.63 | 46.59 | 9.06 | 1 |
| 4 | 1580.8 | 144.16 | 54.16 | 62.34 | 1.64 | 2 |
| 4 | 1581.2 | 172.91 | 82.91 | 60.77 | 1.79 | 2 |
| 4 | 1583.9 | 74.05 | 344.05 | 32.46 | 4.12 | 2 |
| 4 | 1584.5 | 254.84 | 164.84 | 4.81 | 4.74 | 2 |
| 4 | 1584.8 | 260.35 | 170.35 | 4.81 | 4.87 | 2 |
| 4 | 1585.3 | 63.02 | 333.02 | 35.75 | 6.84 | 2 |
| 4 | 1585.6 | 60.26 | 330.26 | 41.63 | 2.74 | 2 |
| 4 | 1586.0 | 248.14 | 158.14 | 18.56 | 3.36 | 2 |
| 4 | 1587.6 | 37.02 | 307.02 | 26.75 | 7.22 | 2 |
| 4 | 1588.0 | 93.74 | 3.74 | 23.36 | 0.30 | 2 |
| 4 | 1588.7 | 88.23 | 358.23 | 32.46 | 2.99 | 2 |
| 4 | 1588.9 | 233.96 | 143.96 | 32.46 | 2.20 | 2 |
| 4 | 1589.1 | 359.21 | 269.21 | 18.56 | 4.51 | 2 |
| 4 | 1590.1 | 113.44 | 23.44 | 52.35 | 2.98 | 2 |
| 3 | 1593.7 | 170.15 | 80.15 | 64.27 | 3.66 | 2 |
| 3 | 1594.3 | 345.03 | 255.03 | 18.57 | 28.35 | 1 |
| 3 | 1594.4 | 103.59 | 13.59 | 44.53 | 2.61 | 2 |
| 3 | 1594.7 | 96.50 | 6.50 | 44.53 | 3.48 | 2 |
| 3 | 1595.1 | 287.13 | 197.13 | 44.53 | 3.48 | 2 |

Note: Unit—lithologic unit as shown on Figure 3. Type—Fracture type: 1—Open; 2—Healed/closed; 3—Partially open; 4—Undetermined.

TABLE 4A. BOREHOLE BREAKOUT ORIENTATIONS AND APERTURES DETERMINED FROM ANALYSES OF THE ACOUSTIC IMAGE LOG DATA

| Depth (m) | Azimuth (°) | Tilt (°) | Length (m) | Opening (°) | Type |
|-----------|-------------|----------|------------|-------------|------|
| 1288.95 | 157.94 | 0.33 | 0.48 | 58.29 | 1 |
| 1288.98 | 331.64 | -0.92 | 0.58 | 66.17 | 1 |
| 1289.81 | 161.49 | 0.49 | 1.01 | 54.35 | 1 |
| 1289.89 | 337.94 | -0.09 | 0.86 | 55.54 | 1 |
| 1290.74 | 334.79 | -0.7 | 0.67 | 62.23 | 1 |
| 1290.74 | 146.91 | 1.04 | 0.66 | 56.72 | 1 |
| 1350.30 | 277.68 | -0.01 | 2.10 | 64.6 | 1 |
| 1350.38 | 101.23 | 0.21 | 1.96 | 70.5 | 1 |
| 1354.10 | 89.41 | -1.65 | 0.95 | 76.41 | 1 |
| 1354.10 | 268.62 | 1.65 | 0.95 | 69.32 | 1 |
| 1394.63 | 129.19 | -1 | 1.38 | 54.35 | 1 |
| 1394.64 | 317.66 | 1.09 | 1.38 | 43.33 | 1 |
| 1401.81 | 320.22 | 0.04 | 2.18 | 57.11 | 1 |
| 1401.82 | 140.61 | 0.51 | 2.16 | 51.6 | 1 |
| 1452.79 | 150.07 | -0.45 | 1.06 | 63.81 | 1 |
| 1452.82 | 332.43 | 0.23 | 1.11 | 69.72 | 1 |
| 1481.78 | 321.6 | 0.07 | 2.12 | 62.63 | 1 |
| 1481.78 | 140.61 | -0.07 | 2.12 | 63.81 | 1 |
| 1498.23 | 313.92 | -0.08 | 5.21 | 80.35 | 1 |
| 1498.24 | 145.73 | 0.06 | 5.19 | 86.65 | 1 |
| 1502.50 | 149.28 | 0.16 | 2.59 | 111.07 | 1 |
| 1502.51 | 330.07 | -0.24 | 2.61 | 80.74 | 1 |
| 1506.10 | 314.31 | -0.05 | 2.89 | 78.77 | 1 |
| 1506.10 | 145.73 | 0.33 | 2.90 | 85.08 | 1 |
| 1511.75 | 137.46 | -0.03 | 7.28 | 97.29 | 1 |
| 1511.76 | 317.07 | -0.08 | 7.30 | 90.59 | 1 |
| 1520.98 | 306.04 | 0.12 | 9.19 | 84.68 | 1 |
| 1520.98 | 137.46 | 0.07 | 9.21 | 91.77 | 1 |
| 1574.64 | 289.5 | -0.96 | 1.20 | 55.14 | 1 |
| 1574.64 | 108.32 | -0.82 | 1.19 | 48.84 | 1 |
| 1291.36 | 330.46 | -0.15 | 0.52 | 59.87 | 2 |
| 1291.36 | 152.04 | 0.15 | 0.52 | 51.6 | 2 |
| 1292.12 | 149.67 | -2.15 | 0.74 | 58.69 | 2 |
| 1292.14 | 332.82 | 1.91 | 0.76 | 58.29 | 2 |
| 1292.86 | 158.73 | 0.73 | 0.48 | 55.54 | 2 |
| 1292.93 | 334 | -0.27 | 0.58 | 44.51 | 2 |
| 1298.41 | 154.4 | -6.52 | 0.23 | 42.93 | 2 |
| 1298.49 | 337.55 | 4.7 | 0.27 | 64.2 | 2 |
| 1306.10 | 201.86 | -3.62 | 0.11 | 38.99 | 2 |
| 1306.10 | 347.4 | 8.59 | 0.14 | 42.93 | 2 |
| 1306.78 | 187.88 | -4.1 | 0.22 | 47.26 | 2 |
| 1306.80 | 357.64 | 3.38 | 0.27 | 42.93 | 2 |
| 1343.38 | 163.85 | 0.04 | 1.40 | 58.29 | 2 |
| 1343.38 | 346.61 | 0.11 | 1.40 | 45.69 | 2 |
| 1348.45 | 161.49 | -8.64 | 0.27 | 67.75 | 2 |
| 1348.45 | 348.18 | 4.39 | 0.27 | 61.44 | 2 |
| 1374.11 | 144.55 | 1.35 | 0.60 | 33.48 | 2 |
| 1374.17 | 317.07 | -1.18 | 0.58 | 25.21 | 2 |
| 1374.95 | 137.86 | 2.25 | 0.46 | 37.81 | 2 |
| 1374.96 | 304.46 | -4.51 | 0.54 | 34.66 | 2 |

(continued)

TABLE 4A. BOREHOLE BREAKOUT ORIENTATIONS AND APERTURES DETERMINED FROM ANALYSES OF THE ACOUSTIC IMAGE LOG DATA (continued)

| Depth (m) | Azimuth (°) | Tilt (°) | Length (m) | Opening (°) | Type |
|-----------|-------------|----------|------------|-------------|------|
| 1376.09 | 143.96 | -1.29 | 0.53 | 38.99 | 2 |
| 1376.09 | 317.86 | 1.29 | 0.53 | 40.18 | 2 |
| 1380.77 | 141.6 | -0.99 | 0.50 | 61.05 | 2 |
| 1380.77 | 315.89 | 0.99 | 0.50 | 55.93 | 2 |
| 1381.55 | 110.09 | 0.8 | 0.72 | 47.66 | 2 |
| 1381.55 | 311.75 | -0.8 | 0.72 | 53.96 | 2 |
| 1383.53 | 144.35 | 2.45 | 0.96 | 35.84 | 2 |
| 1383.53 | 316.67 | -2.45 | 0.96 | 34.66 | 2 |
| 1458.71 | 323.17 | 3.08 | 0.36 | 33.48 | 2 |
| 1458.71 | 145.73 | -3.08 | 0.36 | 30.72 | 2 |
| 1459.44 | 154.99 | -0.27 | 0.52 | 27.96 | 2 |
| 1459.44 | 325.34 | 0.27 | 0.52 | 27.57 | 2 |
| 1469.44 | 155.58 | -0.81 | 0.61 | 33.09 | 2 |
| 1469.45 | 326.91 | 0.46 | 0.64 | 35.05 | 2 |
| 1470.24 | 148.88 | 0.27 | 0.74 | 36.24 | 2 |
| 1470.26 | 327.7 | 0.21 | 0.76 | 27.96 | 2 |
| 1478.53 | 138.05 | 3.29 | 0.34 | 27.96 | 2 |
| 1478.54 | 321.4 | 2.54 | 0.35 | 24.81 | 2 |
| 1484.41 | 327.31 | 0.53 | 0.37 | 41.75 | 2 |
| 1484.42 | 139.82 | -0.5 | 0.39 | 40.18 | 2 |
| 1486.77 | 145.73 | 0.05 | 1.16 | 41.75 | 2 |
| 1486.77 | 322.39 | -0.05 | 1.16 | 35.05 | 2 |
| 1487.59 | 119.54 | 1.91 | 0.43 | 37.42 | 2 |
| 1487.59 | 307.81 | -1.91 | 0.43 | 26.39 | 2 |
| 1488.48 | 293.24 | 1.4 | 0.78 | 55.54 | 2 |
| 1488.48 | 140.42 | -1.4 | 0.78 | 59.47 | 2 |
| 1490.88 | 311.75 | 0.31 | 1.32 | 82.32 | 2 |
| 1490.88 | 136.87 | -0.31 | 1.32 | 86.26 | 2 |
| 1492.83 | 149.08 | -0.85 | 1.62 | 78.38 | 2 |
| 1492.83 | 311.16 | 0.85 | 1.62 | 74.84 | 2 |
| 1494.45 | 135.89 | 1.49 | 1.23 | 74.84 | 2 |
| 1494.46 | 313.52 | 0.62 | 1.23 | 73.26 | 2 |
| 1504.20 | 148.1 | 0.38 | 0.52 | 65.38 | 2 |
| 1504.20 | 330.07 | -0.38 | 0.52 | 58.29 | 2 |
| 1525.74 | 134.31 | 2.16 | 0.19 | 76.41 | 2 |
| 1525.74 | 306.83 | -2.16 | 0.19 | 61.44 | 2 |
| 1527.11 | 127.22 | -0.05 | 1.58 | 81.93 | 2 |
| 1527.11 | 293.83 | 0.05 | 1.58 | 72.47 | 2 |
| 1553.31 | 330.66 | -4.13 | 0.38 | 15.36 | 2 |
| 1553.32 | 131.95 | 4.13 | 0.38 | 16.54 | 2 |
| 1556.81 | 99.06 | 1.57 | 0.21 | 29.54 | 2 |
| 1556.81 | 289.5 | -1.57 | 0.21 | 27.57 | 2 |
| 1557.82 | 127.02 | 2.12 | 0.45 | 33.48 | 2 |
| 1557.82 | 302.69 | -2.12 | 0.45 | 38.99 | 2 |
| 1558.35 | 292.65 | -3.32 | 0.09 | 62.63 | 2 |
| 1558.37 | 109.3 | 2.89 | 0.12 | 42.93 | 2 |
| 1595.93 | 135.3 | 0.27 | 0.73 | 98.86 | 2 |
| 1595.93 | 303.48 | -0.27 | 0.73 | 97.29 | 2 |

Note: Type: 1—well developed; 2—moderately well developed.

TABLE 4B. DRILLING-INDUCED TENSILE FRACTURE ORIENTATIONS AND APERTURES DETERMINED FROM ANALYSIS OF THE ACOUSTIC IMAGE LOG DATA

| Depth (m) | Azimuth (°) | Tilt (°) | Length (m) |
|-----------|-------------|----------|------------|
| 1299.39 | 352.12 | -5.38 | 0.51 |
| 1299.39 | 156.76 | 5.38 | 0.51 |
| 1300.49 | 159.12 | 1.89 | 0.37 |
| 1300.49 | 339.12 | -1.89 | 0.37 |
| 1302.33 | 343.85 | 0.00 | 0.04 |
| 1302.33 | 163.85 | 0.00 | 0.04 |
| 1302.68 | 343.85 | 0.00 | 0.09 |
| 1302.68 | 163.85 | 0.00 | 0.09 |
| 1304.77 | 202.84 | 7.94 | 0.30 |
| 1304.77 | 22.84 | -7.94 | 0.30 |
| 1307.62 | 208.36 | -5.83 | 0.29 |
| 1307.62 | 28.36 | 5.83 | 0.29 |
| 1311.00 | 110.28 | 1.83 | 0.52 |
| 1311.00 | 290.28 | -1.83 | 0.52 |
| 1323.52 | 144.55 | 1.80 | 0.26 |
| 1323.52 | 324.55 | -1.80 | 0.26 |
| 1323.72 | 352.12 | 0.00 | 0.18 |
| 1323.72 | 172.12 | 0.00 | 0.18 |
| 1324.23 | 332.04 | -0.39 | 0.20 |
| 1324.23 | 152.04 | 0.39 | 0.20 |
| 1325.44 | 215.84 | 7.07 | 0.12 |
| 1325.44 | 35.84 | -7.07 | 0.12 |
| 1326.56 | 50.42 | -0.93 | 0.15 |
| 1326.56 | 230.42 | 0.93 | 0.15 |
| 1327.64 | 244.60 | 2.32 | 0.15 |
| 1327.64 | 64.60 | -2.32 | 0.15 |
| 1329.49 | 68.93 | 0.00 | 0.15 |
| 1329.49 | 248.93 | 0.00 | 0.15 |
| 1330.01 | 85.47 | 0.00 | 0.33 |
| 1330.01 | 265.47 | 0.00 | 0.33 |
| 1331.17 | 97.29 | 1.52 | 0.49 |
| 1331.17 | 277.29 | -1.52 | 0.49 |
| 1331.65 | 242.23 | 10.49 | 0.30 |
| 1331.65 | 62.23 | -10.49 | 0.30 |
| 1332.82 | 81.93 | -0.09 | 0.84 |
| 1332.82 | 261.93 | 0.09 | 0.84 |
| 1333.67 | 40.18 | 0.78 | 0.63 |
| 1333.67 | 220.18 | -0.78 | 0.63 |
| 1339.80 | 202.06 | 0.14 | 2.86 |
| 1339.80 | 22.06 | -0.14 | 2.86 |
| 1347.93 | 90.20 | 1.35 | 0.16 |
| 1347.93 | 270.20 | -1.35 | 0.16 |
| 1364.12 | 242.23 | -0.86 | 0.16 |
| 1364.12 | 62.23 | 0.86 | 0.16 |
| 1364.42 | 17.33 | 0.00 | 0.16 |
| 1364.42 | 197.33 | 0.00 | 0.16 |
| 1364.99 | 192.60 | 1.43 | 0.38 |
| 1364.99 | 12.60 | -1.43 | 0.38 |
| 1367.91 | 115.01 | -1.25 | 0.61 |
| 1367.91 | 295.01 | 1.25 | 0.61 |
| 1368.40 | 27.57 | -0.35 | 0.17 |
| 1368.40 | 207.57 | 0.35 | 0.17 |
| 1381.63 | 207.57 | 0.00 | 0.18 |
| 1381.63 | 27.57 | 0.00 | 0.18 |
| 1389.77 | 17.33 | 0.81 | 0.17 |
| 1389.77 | 197.33 | -0.81 | 0.17 |
| 1398.72 | 98.47 | -0.48 | 0.13 |
| 1398.72 | 278.47 | 0.48 | 0.13 |
| 1403.70 | 152.82 | 3.38 | 0.47 |
| 1403.70 | 332.82 | -3.38 | 0.47 |
| 1404.78 | 298.16 | -2.73 | 0.46 |
| 1404.78 | 118.16 | 2.73 | 0.46 |

(continued)

TABLE 4B. DRILLING-INDUCED TENSILE FRACTURE ORIENTATIONS AND APERTURES DETERMINED FROM ANALYSIS OF THE ACOUSTIC IMAGE LOG DATA

| (continued) | | | |
|-------------|-------------|----------|------------|
| Depth (m) | Azimuth (°) | Tilt (°) | Length (m) |
| 1405.74 | 195.36 | 4.05 | 0.14 |
| 1405.74 | 15.36 | -4.05 | 0.14 |
| 1408.10 | 192.21 | 2.33 | 0.18 |
| 1408.10 | 12.21 | -2.33 | 0.18 |
| 1412.24 | 352.12 | -2.65 | 0.21 |
| 1412.24 | 172.12 | 2.65 | 0.21 |
| 1413.28 | 183.94 | 1.33 | 0.93 |
| 1413.28 | 3.94 | -1.33 | 0.93 |
| 1413.82 | 174.88 | -0.54 | 0.11 |
| 1413.82 | 354.88 | 0.54 | 0.11 |
| 1415.49 | 200.88 | 3.47 | 0.59 |
| 1415.49 | 20.88 | -3.47 | 0.59 |
| 1418.24 | 165.82 | 2.40 | 0.35 |
| 1418.24 | 345.82 | -2.40 | 0.35 |
| 1432.66 | 326.91 | 1.47 | 0.09 |
| 1432.66 | 146.91 | -1.47 | 0.09 |
| 1433.21 | 211.90 | 0.00 | 0.06 |
| 1433.21 | 31.90 | 0.00 | 0.06 |
| 1437.86 | 186.30 | 0.68 | 0.12 |
| 1437.86 | 6.30 | -0.68 | 0.12 |
| 1438.12 | 11.82 | 0.00 | 0.05 |
| 1438.12 | 191.82 | 0.00 | 0.05 |
| 1439.22 | 162.28 | 3.95 | 0.26 |
| 1439.22 | 342.28 | -3.95 | 0.26 |
| 1439.83 | 166.61 | -2.38 | 0.66 |
| 1439.83 | 346.61 | 2.38 | 0.66 |
| 1440.29 | 349.37 | -2.80 | 0.15 |
| 1440.29 | 169.37 | 2.80 | 0.15 |
| 1440.34 | 345.82 | -4.01 | 0.22 |
| 1440.34 | 165.82 | 4.01 | 0.22 |
| 1440.44 | 174.09 | 0.98 | 0.14 |
| 1440.44 | 354.09 | -0.98 | 0.14 |
| 1440.72 | 350.55 | 0.97 | 0.43 |
| 1440.72 | 170.55 | -0.97 | 0.43 |
| 1441.63 | 196.54 | 0.75 | 0.37 |
| 1441.63 | 16.54 | -0.75 | 0.37 |
| 1442.80 | 206.78 | 4.26 | 0.12 |
| 1442.80 | 26.78 | -4.26 | 0.12 |
| 1443.09 | 11.82 | 0.00 | 0.10 |
| 1443.09 | 191.82 | 0.00 | 0.10 |
| 1445.03 | 341.09 | 0.00 | 0.18 |
| 1445.03 | 161.09 | 0.00 | 0.18 |
| 1445.39 | 345.03 | -2.98 | 0.32 |
| 1445.39 | 165.03 | 2.98 | 0.32 |
| 1446.40 | 162.28 | -1.65 | 0.13 |
| 1446.40 | 342.28 | 1.65 | 0.13 |
| 1448.69 | 324.95 | -0.52 | 0.11 |
| 1448.69 | 144.95 | 0.52 | 0.11 |
| 1450.85 | 18.91 | 0.00 | 0.15 |
| 1450.85 | 198.91 | 0.00 | 0.15 |
| 1451.89 | 176.46 | 0.85 | 0.41 |
| 1451.89 | 356.46 | -0.85 | 0.41 |
| 1458.10 | 251.29 | 2.07 | 0.43 |
| 1458.10 | 71.29 | -2.07 | 0.43 |
| 1464.59 | 55.54 | 0.38 | 0.52 |
| 1464.59 | 235.54 | -0.38 | 0.52 |
| 1466.60 | 155.58 | -0.06 | 1.41 |
| 1466.60 | 335.58 | 0.06 | 1.41 |
| 1467.83 | 339.12 | 0.57 | 0.34 |
| 1467.83 | 159.12 | -0.57 | 0.34 |
| 1468.43 | 334.00 | 1.55 | 0.09 |

(continued)

TABLE 4B. DRILLING-INDUCED TENSILE FRACTURE ORIENTATIONS AND APERTURES DETERMINED FROM ANALYSIS OF THE ACOUSTIC IMAGE LOG DATA

| (continued) | | | |
|-------------|-------------|----------|------------|
| Depth (m) | Azimuth (°) | Tilt (°) | Length (m) |
| 1468.43 | 154.00 | -1.55 | 0.09 |
| 1472.63 | 337.55 | 0.97 | 0.23 |
| 1472.63 | 157.55 | -0.97 | 0.23 |
| 1473.20 | 231.20 | 0.66 | 0.21 |
| 1473.20 | 51.20 | -0.66 | 0.21 |
| 1473.68 | 229.63 | -0.37 | 0.37 |
| 1473.68 | 49.63 | 0.37 | 0.37 |
| 1478.70 | 293.04 | 0.24 | 0.25 |
| 1478.70 | 113.04 | -0.24 | 0.25 |
| 1478.91 | 352.91 | -0.29 | 0.27 |
| 1478.91 | 172.91 | 0.29 | 0.27 |
| 1484.98 | 116.59 | 1.32 | 0.25 |
| 1484.98 | 296.59 | -1.32 | 0.25 |
| 1485.71 | 165.82 | 1.13 | 0.12 |
| 1485.71 | 345.82 | -1.13 | 0.12 |
| 1535.45 | 335.58 | 0.00 | 0.60 |
| 1535.45 | 155.58 | 0.00 | 0.60 |
| 1535.99 | 331.25 | 0.00 | 0.23 |
| 1535.99 | 151.25 | 0.00 | 0.23 |
| 1536.86 | 155.58 | 0.67 | 0.52 |
| 1536.86 | 335.58 | -0.67 | 0.52 |
| 1537.80 | 77.59 | 0.82 | 0.07 |
| 1537.80 | 257.59 | -0.82 | 0.07 |
| 1539.43 | 199.30 | -2.43 | 1.20 |
| 1539.43 | 19.30 | 2.43 | 1.20 |
| 1540.58 | 50.42 | 0.81 | 0.17 |
| 1540.58 | 230.42 | -0.81 | 0.17 |
| 1540.83 | 57.51 | 0.00 | 0.25 |
| 1540.83 | 237.51 | 0.00 | 0.25 |
| 1541.42 | 163.85 | 0.95 | 0.23 |
| 1541.42 | 343.85 | -0.95 | 0.23 |
| 1541.93 | 57.51 | 0.44 | 0.31 |
| 1541.93 | 237.51 | -0.44 | 0.31 |
| 1544.10 | 345.03 | 0.81 | 0.17 |
| 1544.10 | 165.03 | -0.81 | 0.17 |
| 1545.07 | 150.07 | -0.26 | 0.82 |
| 1545.07 | 329.28 | 0.26 | 0.82 |
| 1546.00 | 60.26 | 0.96 | 0.60 |
| 1546.00 | 240.26 | -0.96 | 0.60 |
| 1546.64 | 80.35 | -0.13 | 0.45 |
| 1546.64 | 260.35 | 0.13 | 0.45 |
| 1547.60 | 268.62 | -1.37 | 0.30 |
| 1547.60 | 88.62 | 1.37 | 0.30 |
| 1548.12 | 226.87 | 6.52 | 0.45 |
| 1548.12 | 46.87 | -6.52 | 0.45 |
| 1548.58 | 269.02 | -1.69 | 0.33 |
| 1548.58 | 89.02 | 1.69 | 0.33 |
| 1549.14 | 269.02 | -2.83 | 0.20 |
| 1549.14 | 89.02 | 2.83 | 0.20 |
| 1549.18 | 233.96 | -2.14 | 0.27 |
| 1549.18 | 53.96 | 2.14 | 0.27 |
| 1550.00 | 82.71 | 4.86 | 0.17 |
| 1550.00 | 262.71 | -4.86 | 0.17 |
| 1550.16 | 345.03 | 0.47 | 0.29 |
| 1550.16 | 165.03 | -0.47 | 0.29 |
| 1551.27 | 333.22 | -0.82 | 0.26 |
| 1551.27 | 153.22 | 0.82 | 0.26 |
| 1553.05 | 309.19 | 4.29 | 0.10 |
| 1553.05 | 129.19 | -4.29 | 0.10 |
| 1554.53 | 217.42 | 0.00 | 0.54 |
| 1554.53 | 37.42 | 0.00 | 0.54 |

(continued)

TABLE 4B. DRILLING-INDUCED TENSILE FRACTURE ORIENTATIONS AND APERTURES DETERMINED FROM ANALYSIS OF THE ACOUSTIC IMAGE LOG DATA

| (continued) | | | |
|-------------|-------------|----------|------------|
| Depth (m) | Azimuth (°) | Tilt (°) | Length (m) |
| 1555.22 | 221.36 | 0.53 | 0.26 |
| 1555.22 | 41.36 | -0.53 | 0.26 |
| 1555.49 | 320.22 | 1.05 | 0.13 |
| 1555.49 | 140.22 | -1.05 | 0.13 |
| 1557.13 | 52.78 | -0.16 | 0.49 |
| 1557.13 | 232.78 | 0.16 | 0.49 |
| 1559.97 | 169.37 | 2.09 | 1.31 |
| 1559.97 | 349.37 | -2.09 | 1.31 |
| 1561.15 | 206.00 | -0.42 | 0.33 |
| 1561.15 | 26.00 | 0.42 | 0.33 |
| 1561.51 | 29.54 | 0.97 | 1.07 |
| 1561.73 | 213.09 | -1.11 | 0.62 |
| 1563.12 | 233.17 | -0.95 | 0.52 |
| 1563.12 | 53.17 | 0.95 | 0.52 |
| 1563.45 | 170.94 | -0.28 | 0.70 |
| 1563.45 | 350.94 | 0.28 | 0.70 |
| 1563.65 | 323.76 | 0.53 | 0.37 |
| 1563.65 | 143.76 | -0.53 | 0.37 |
| 1563.74 | 13.79 | -1.26 | 0.39 |
| 1563.74 | 193.79 | 1.26 | 0.39 |
| 1564.51 | 199.30 | 2.76 | 0.20 |
| 1564.51 | 19.30 | -2.76 | 0.20 |
| 1564.70 | 161.49 | -1.09 | 0.20 |
| 1564.70 | 342.28 | 0.78 | 0.18 |
| 1565.08 | 211.90 | 1.86 | 0.38 |
| 1565.08 | 31.90 | -1.86 | 0.38 |
| 1568.99 | 354.88 | 1.26 | 0.11 |
| 1568.99 | 174.88 | -1.26 | 0.11 |
| 1569.28 | 181.18 | 0.00 | 0.19 |
| 1569.28 | 1.18 | 0.00 | 0.19 |
| 1570.11 | 341.09 | 1.68 | 0.75 |
| 1570.11 | 161.09 | -1.68 | 0.75 |
| 1571.95 | 214.66 | 8.63 | 0.25 |
| 1571.95 | 34.66 | -8.63 | 0.25 |
| 1572.31 | 61.05 | 2.39 | 0.26 |
| 1572.31 | 241.05 | -2.39 | 0.26 |
| 1577.39 | 137.46 | -1.52 | 0.41 |
| 1577.39 | 317.46 | 1.52 | 0.41 |
| 1578.14 | 172.91 | 0.20 | 0.70 |
| 1578.14 | 352.91 | -0.20 | 0.70 |
| 1579.33 | 145.73 | -0.17 | 0.35 |
| 1579.33 | 325.73 | 0.17 | 0.35 |
| 1579.64 | 112.65 | 0.52 | 0.15 |
| 1579.64 | 292.65 | -0.52 | 0.15 |
| 1580.10 | 144.55 | -2.29 | 0.27 |
| 1580.10 | 324.55 | 2.29 | 0.27 |
| 1580.45 | 340.31 | 0.86 | 0.25 |
| 1580.45 | 160.31 | -0.86 | 0.25 |
| 1583.81 | 348.18 | 1.07 | 0.26 |
| 1583.81 | 168.18 | -1.07 | 0.26 |
| 1584.58 | 32.69 | 1.58 | 0.17 |
| 1584.58 | 212.69 | -1.58 | 0.17 |
| 1585.11 | 218.21 | -0.17 | 0.48 |
| 1585.11 | 38.21 | 0.17 | 0.48 |
| 1586.28 | 42.93 | 0.19 | 0.31 |
| 1586.28 | 222.93 | -0.19 | 0.31 |
| 1588.32 | 161.88 | 0.27 | 0.59 |
| 1588.32 | 341.88 | -0.27 | 0.59 |
| 1588.85 | 211.90 | -0.37 | 0.43 |
| 1588.85 | 31.90 | 0.37 | 0.43 |
| 1592.22 | 10.24 | 0.00 | 0.15 |
| 1592.22 | 190.24 | 0.00 | 0.15 |

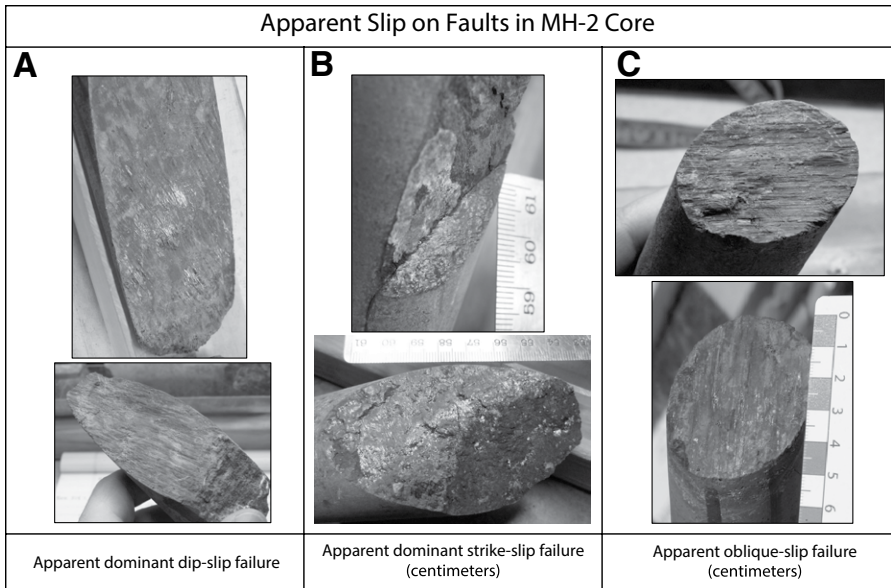


Figure 8. Examples of faults in the MH-2 core. (A, B) Slickenlines are expressed as green-gray surfaces on thin slip surfaces. (C) Fault dip is measured as the fault plane-core axis angle, and because the core is nearly vertical, this equates to fault dip. The rake of the slip vectors is measured from the strike. Some of the faults are patchy, with highly reflective surfaces interspersed with altered zones.

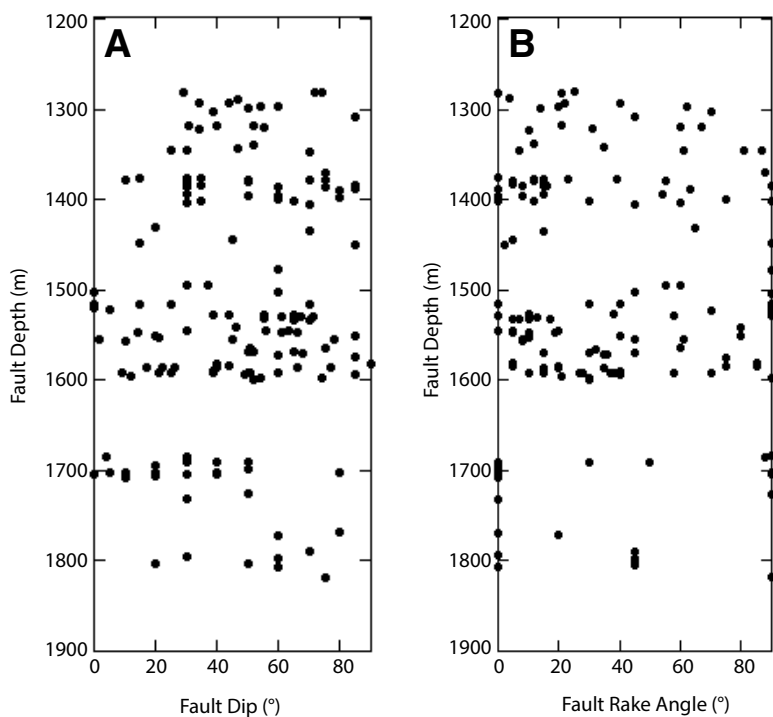
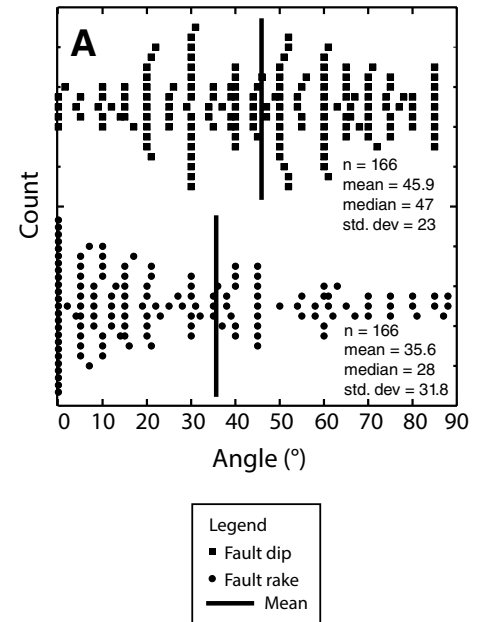


Figure 9. Fault slip data plotted as a function of depth. (A) Fault dip distribution over the zone of interest. Four zones of faulting are present in the core, and there is little to no concentration of fault dip as a function of depth. (B) Fault slip vector rake angles as a function of depth.

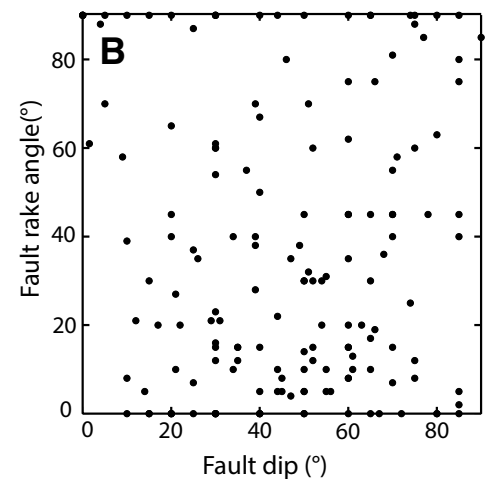


Figure 10. (A, B) Dot plots and simple statistics of the fault data. Fault dips have a mean value of 45° ($\pm 23^\circ$). Fault slip vectors exhibit a strong oblique slip component, with a mean value of 35° , median of 28° ($\pm 32^\circ$). Note the large number of pure strike-slip vectors. $N = 166$. Std. dev—standard deviation.

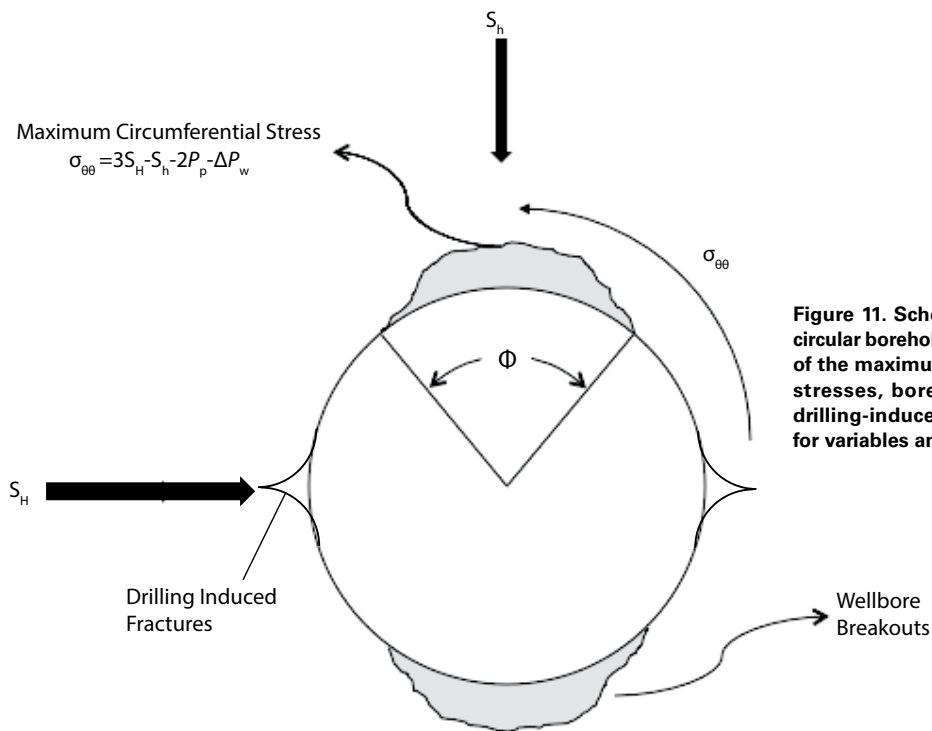


Figure 11. Schematic plan view of a circular borehole with the orientations of the maximum and least horizontal stresses, borehole breakouts, and drilling-induced fractures. (See text for variables and explanation.)

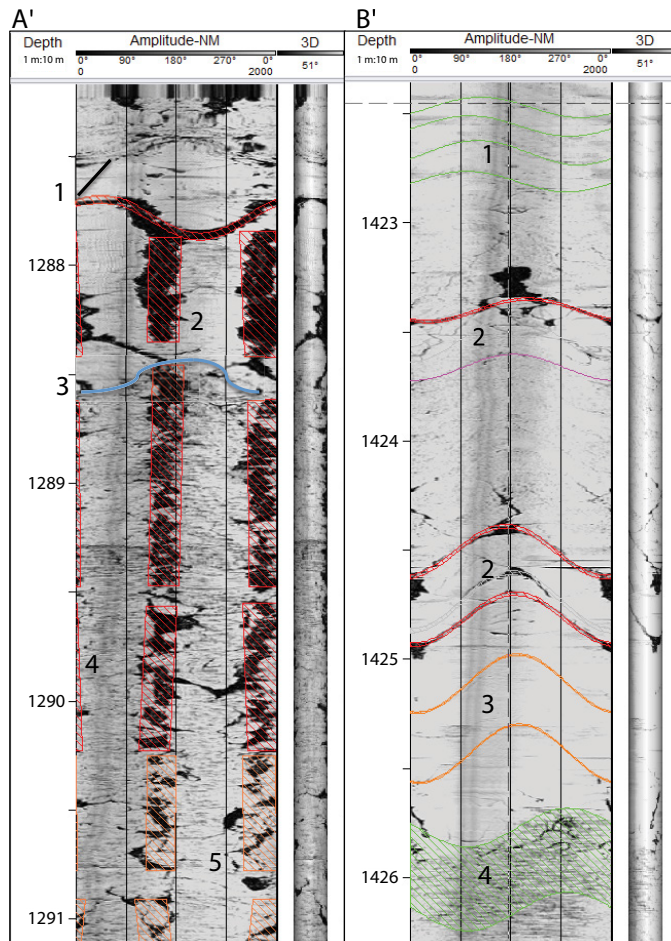


Figure 12. Example of an acoustic borehole image log showing examples of structures interpreted from the sonic image log. Images are shown for travelttime and amplitude. On the left side of the figures the image log is an unrolled view from 0° to 360°, and on the right side is a view of the log as a pseudocore from 51° perspective. 3D—three dimensional; NM—integrated amplitude. (A) Region from 1287.5 to 1291 m shows the expression of: 1—natural openings possibly along a lithologic boundary; 2—lithologic boundary; 3—well-developed borehole breakout; 4—moderately developed breakout; 5—drilling-induced tensile fracture. (B) Region from 1422.5 to 1426.1 m depth that shows the expression of: 1—lithologic boundary or fractures along a cooling unit boundary; 2, 3—shallow and steeply dipping natural fractures; 4—naturally occurring void spaces and a zone of alteration.

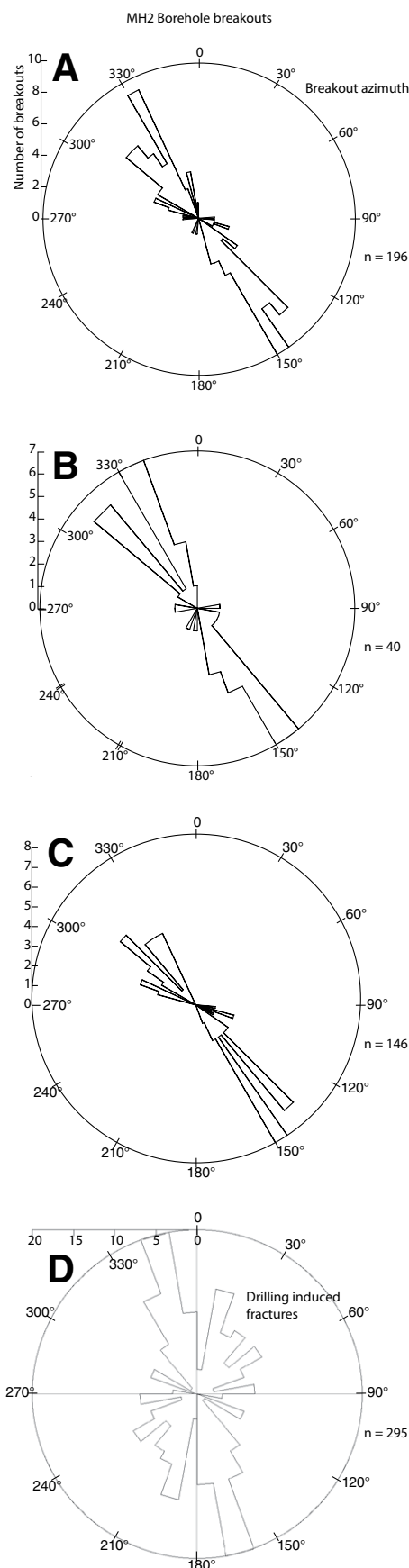


Figure 13. Borehole breakout results rose diagrams. (A) Summary rose diagram for the orientations of the borehole breakouts in the region over which the acoustic image log data were collected. (B) Rose diagram of borehole breakout fractures over the depth region of 1280–1401 m. (C) Rose diagram of borehole breakout fractures over the depth region of 1405 m to 1600 m. (D) Drilling-induced tensile fracture orientations for the lower 540 m of the MH-2 borehole.

basin axis (Fig. 14). The nearest stress orientation indicators based on breakout data and earthquake focal mechanisms are from the Basin and Range in Nevada and S_H orientations from the Columbia River Basalt in Oregon (Heidbach et al., 2008). In Oregon, S_H orientations are predominantly oriented north-northeast. The S_H orientations in the Basin and Range in northern Nevada are similar to the S_H orientation in MH-2, $\sim 020^\circ$. The trend of the western SRP is at a high angle to Basin and Range structures, especially when compared to those closest to southern Idaho and the western SRP (Fig. 14). The orientation of S_h (minimum horizontal stress) determined from the drilling-induced fractures is $157^\circ \pm 21^\circ$, or an S_H orientation of 67° (Fig. 13D).

Stress Magnitudes

We estimate the stress magnitudes from the borehole breakout and drilling-induced

tensile fracture data using the methods outlined in Zoback et al. (2003), Zoback (2010), and Schmitt et al. (2012). We start the analyses by assuming the rock mass is critically stressed (Barton et al., 1995), i.e., for a given region in the crust there are enough fractures and faults oriented such that they are at or near shear failure based on static equilibrium (Jaeger and Cook, 1979). Our data (Figs. 3H, 3I, 8, and 9) indicate that four or five orientation concentrations of fractures and faults exist over the sampled interval and that the range of fracture and fault orientations and slip orientations validates the assumption that the rocks are highly fractured with a range of potential slip plane orientations.

First, the vertical compressive stress at a given depth (S_v) is given by

$$S_v = \int_0^h \rho(h)gdh, \quad (2)$$

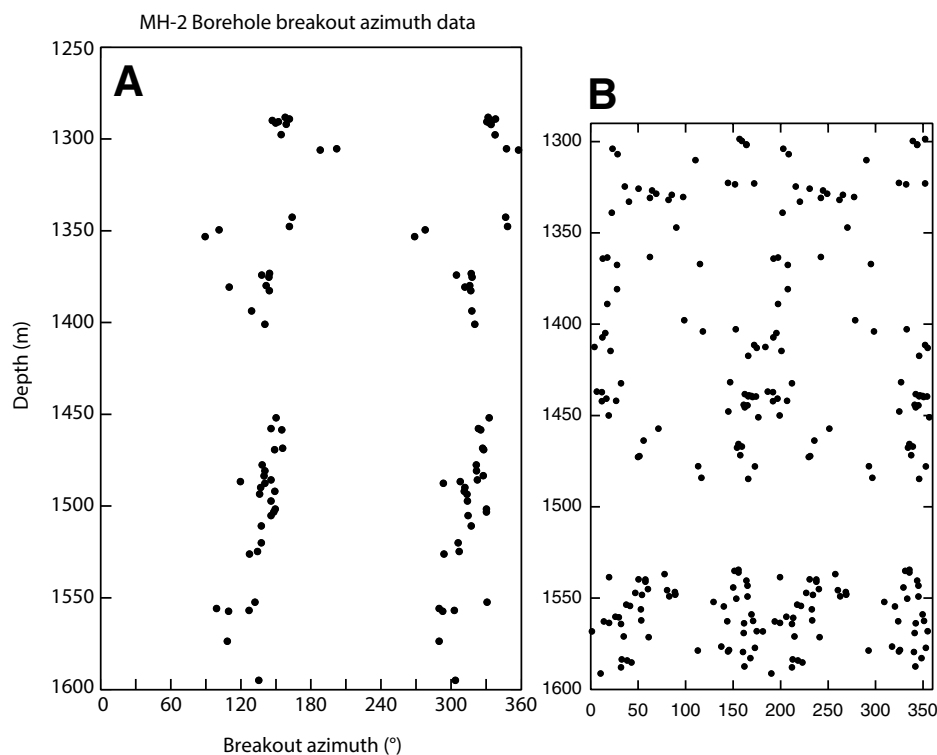


Figure 14. (A) Orientation of the borehole breakouts as a function of depth in the borehole. (B) Orientation of drilling-induced tensile fractures as a function of depth.

where $\rho(h)$ is the mean bulk density, g is the acceleration due to gravity, and h is the depth of investigation. In the case of the MH-2 drillhole we use the laboratory measured densities (Fig. 3) for the basalts, a value of 2.0 g/cm³ for the ~650 m of lacustrine deposits above the ZOI, and a hydrostatic pore pressure gradient of 9.8 MPa/km.

To constrain the values of S_h (Equation 3), we assume that the basalt formations are part of the critically stressed crust (Barton et al., 1995), for which Jaeger and Cook (1979) showed:

$$\frac{S_1 - P_p}{S_3 - P_p} = \left[(\mu^2 + 1)^{1/2} + \mu \right]^2 \quad (3)$$

We start with the normal fault case, consistent with the regional tectonics with the maximum principal compression $S_1 = S_v$ and the minimum principal compression $S_3 = S_h$. Using the estimated S_v from Equation 2, we then calculate the stresses for 3 values of the coefficient of friction: $\mu = 0.6, 0.8,$ and 1.0 ; these values yield $S_h = 15.6$ MPa/km, 13.8 MPa/km, and 13 MPa/km, respectively.

In a normal faulting regime the maximum and minimum compressions are respectively S_v and S_h ; S_H is intermediate to these. Therefore, finding the magnitude of S_H provides additional evidence to support the geologically based contention that the rock mass is subject to a normal faulting environment. Here we use the width of the breakouts together with laboratory derived values of the rock strength to constrain the magnitude of S_H . The extent to which a borehole wall deforms and undergoes shear failure is a function of the maximum compressive stress and the strength of the rocks near the borehole wall (e.g., Gough and Bell, 1982; Moos and Zoback, 1990). Where the concentration of circumferential hoop stresses perpendicular to S_H exceed the rock strength, then shear failure occurs when the borehole deforms under in situ stresses. The time strain portion of the deformation takes place as a deepening of the breakout and the width of the breakout remains a function of S_H . The angle of the breakout, ϕ (Fig. 11; Barton et al., 1988; Zoback et al., 2003; Zoback, 2010; Schmitt et al., 2012) is given by:

$$S_H = \left[\frac{(C_0 + 2P_p)}{(1 - 2\cos 2\theta)} \right] - S_h \left[\frac{(1 + 2\cos 2\theta)}{(1 - 2\cos 2\theta)} \right], \quad (4)$$

where $2\theta = \pi - \phi_{rad}$, (5)

where ϕ_{rad} is the angle of wellbore breakout, in radians (Fig. 11), C_0 is the cohesive strength of the rock, and P_p is pore pressure that we estimated from the hydraulic gradient. For a Mohr-Coulomb material with a linear shear failure envelope the cohesion (C_0) is found from:

$$C_0 = \frac{UCS}{\left[2(\mu^2 + 1)^{1/2} + 1 \right]}, \quad (6)$$

where UCS is unconfined compressive strength. We used UCS values from laboratory rock mechanics measurements on the Mountain Home core (Kessler, 2014; Table 5). These UCS data were used to subdivide the ZOI into nine mechanical units (in Kessler, 2014), and this work will be a topic elsewhere. The experimentally determined values of UCS vary considerably, and we determine the range of S_H for low, median, and high values of UCS for each unit.

The total uncertainties for the S_H calculations are also due to the measurement errors for ϕ_{rad} , variations due to the experimentally determined values of UCS, and the likely ranges for μ . We calculate (Fig. 15) a midpoint for the mean value of UCS for each section and $\mu = 0.8$ (Byerlee, 1978). The lower bounds are calculated from the lowest UCS and a μ of 0.6, and the higher bound is for the largest UCS value and a μ of 1.0. (Algebraically, Equation 2 shows that the lowest bound is for a low UCS and high value of μ , and the higher bound is given by the largest UCS and lowest μ , but these do not vary

TABLE 5. UNCONFINED COMPRESSIVE STRENGTH DATA

| Unit | Depth (m bgs) | 1st UCS (Mpa) | 2nd UCS (Mpa) | Average UCS (Mpa) | Standard deviation UCS (Mpa) | Unit average (Mpa) | Standard deviation of UCS for unit |
|------|---------------|---------------|---------------|-------------------|------------------------------|--------------------|------------------------------------|
| 9 | 1289.00 | 127.1 | 77.6 | 102.3 | 24.8 | | |
| 9 | 1295.40 | 76.2 | 106.0 | 91.1 | 14.9 | | |
| 9 | 1305.76 | 132.5 | 147.0 | 139.7 | 7.3 | | |
| 9 | 1312.16 | 86.6 | 100.1 | 93.4 | 6.8 | | |
| 9 | 1322.83 | 133.7 | 133.7 | 133.7 | None | | |
| 9 | 1336.85 | 37.4 | 45.5 | 41.4 | 4.1 | | |
| 9 | 1349.96 | 126.8 | 190.5 | 158.6 | 31.9 | 108.60 | 36.23 |
| 8 | 1363.68 | 22.9 | 22.5 | 22.7 | 0.2 | | |
| 8 | 1375.26 | 43.5 | 45.3 | 44.4 | 0.9 | 33.56 | 10.84 |
| 7 | 1394.16 | 136.8 | 140.9 | 138.9 | 2.1 | | |
| 7 | 1400.25 | 61.8 | 59.0 | 60.4 | 1.4 | | |
| 7 | 1407.87 | 134.6 | 146.1 | 140.4 | 5.8 | | |
| 7 | 1414.27 | 121. | 119.9 | 120.4 | 0.5 | | |
| 7 | 1421.59 | 113.8 | 137.2 | 125.5 | 11.7 | 117.11 | 29.36 |
| 6 | 1436.22 | 147.8 | 133.6 | 140.7 | 7.1 | | |
| 6 | 1448.10 | 109.1 | 114.3 | 111.7 | 2.6 | | |
| 6 | 1457.55 | 152. | 190.6 | 171.3 | 19.3 | | |
| 6 | 1468.53 | 152.4 | ND | 152.4 | None | | |
| 6 | 1471.57 | 188.4 | ND | 188.4 | None | | |
| 6 | 1481.33 | 189.7 | 150.2 | 170.0 | 19.7 | 155.74 | 24.81 |
| 5 | 1484.38 | 70.7 | 64.2 | 67.5 | 3.2 | | |
| 5 | 1497.79 | 42.6 | 51.9 | 47.3 | 4.7 | | |
| 5 | 1503.58 | 52.2 | 52.1 | 52.1 | 0.0 | | |
| 5 | 1512.42 | 40.1 | 42.7 | 41.4 | 1.3 | | |
| 5 | 1517.29 | 36.8 | 36.8 | 36.8 | None | | |
| 5 | 1527.66 | 82.8 | 56.0 | 69.4 | 13.4 | 52.41 | 12.29 |
| 4 | 1532.53 | 155.1 | 172.1 | 163.6 | 8.5 | | |
| 4 | 1542.59 | 184.4 | 125.9 | 155.1 | 29.3 | | |
| 4 | 1548.38 | 111.7 | 109.4 | 110.5 | 1.1 | | |
| 4 | 1549.30 | 137.1 | 107.5 | 122.3 | 14.8 | | |
| 4 | 1557.53 | 166.5 | 147.6 | 157.1 | 9.5 | | |
| 4 | 1564.54 | 116.5 | 125.8 | 121.1 | 4.7 | | |
| 4 | 1575.21 | 162.2 | 141.8 | 152.0 | 10.2 | | |
| 4 | 1586.79 | 181.8 | 163.5 | 172.6 | 9.2 | | |
| 4 | 1589.84 | 87.3 | 97.1 | 92.2 | 4.9 | 138.51 | 26.01 |
| 3 | 1594.71 | 164.6 | 158.7 | 161.7 | 2.9 | | |
| 3 | 1614.53 | 162.9 | 186.3 | 174.6 | 11.7 | | |
| 3 | 1649.88 | 172.1 | 174.5 | 173.3 | 1.2 | | |
| 3 | 1662.99 | 181.4 | 177.5 | 179.5 | 1.9 | | |
| 3 | 1678.84 | 179.1 | 152.5 | 165.8 | 13.3 | | |
| 3 | 1692.55 | 153.1 | 181.0 | 167.0 | 13.9 | 170.31 | 6.01 |
| 2 | 1708.10 | 90.5 | 83.6 | 87.1 | 3.4 | | |
| 2 | 1718.77 | 20.6 | 20.6 | 20.6 | None | | |
| 2 | 1734.62 | 26.4 | 24.6 | 25.5 | 0.9 | 44.39 | 30.25 |
| 1 | 1738.27 | 153.9 | 148.4 | 151.1 | 2.8 | | |
| 1 | 1763.27 | 84.0 | 85.2 | 84.6 | 0.6 | | |
| 1 | 1787.65 | 110.8 | 120.6 | 115.7 | 4.9 | | |
| 1 | 1805.94 | 80.7 | 106.8 | 93.7 | 13.0 | | |
| 1 | 1806.85 | 55.6 | ND | 55.6 | None | | |
| 1 | #REF! | 175.7 | 187.3 | 181.5 | 5.8 | 113.72 | 42.08 |

Note: ND—no data; unit—lithologic unit described in text; 1st UCS—value for first test; 2nd UCS—value for second test; Standard deviation UCS—variation for individual test; Standard deviation of UCS for unit—variation for all tests within lithologic unit.

significantly from the results shown here, and these end members are counterintuitive from a rock mechanics perspective.)

The results of the stress magnitude analyses (Fig. 15) reveal the influence that the rock properties have on stress magnitudes owing to Equations 3 and 5, and we see the ranges of stress magnitudes over the vertical section. The calculations yield mean stresses that are broadly consistent with $S_h < S_H < S_v$, or a dominantly normal fault stress state. The values of S_h vary by 15–20 MPa for the ranges of UCS (Fig. 15), and the strongest horizons exhibit ranges of S_H that approach S_v at depths of 1280–1300 m and 1330–1355 m md, and 1450–1475 m md. Here, the mean values of S_H are approximately equal to or greater than S_v . The horizons from ~1365–1380 m md and 1480–1520 m md are weak and S_H approaches S_h . The sections with the larger S_h values may help explain the presence of oblique slip striations observed in the core (Fig. 9).

This analysis assumes a normal fault stress regime ($S_v > S_H > S_h$), which is broadly consistent

with the regional setting, and it allows us to estimate S_h and S_H based on Equations 3 and 4. In three horizons in the ZOI the upper bound of S_H is as large as or greater than S_v . If these conditions prevail in the rocks in the subsurface, these stresses are consistent with mixed mode, or oblique fault slip. Within the two weak horizons at ~1370 and 1480–1530 m md, S_H approaches S_h which would result in a switch of the orientation of the optimally oriented normal fault from north-northeast striking to north-northwest striking.

A mixed mode strike-slip regime in portions of the section is also indicated by the presence of drilling-induced tensile fractures (Appendix Fig. A1). The presence of tensile fractures in a borehole indicates that $S_H - S_h$ is large enough to induce tensile failure, which is equivalent to a strike-slip stress regime (Zoback, 2010, p. 133). Assuming low thermal stresses, negligible tensile strength (Schultz, 1995), and no excess mudweight, $S_H = 3 S_h - 2 P_p$. Because we have no independent measure of S_h (e.g., from hydrofractures) we cannot constrain the

horizontal stress magnitudes further, other than to infer that $S_H > S_v$.

We assumed a normal hydrostatic gradient for our analysis and recognize that this introduces uncertainty in the calculated S_H values and results in S_H values that are lower bounds for the geothermally charged section at the very bottom of the hole. High geothermal gradient and high bottom-hole temperatures can cause elevated pore pressure (Barker, 1972; Luo and Vasseur, 1992; Zoback, 2010; Swarbrick, 2012) and are likely to exist at depth in the MH-2 site (Nielson et al., 2012, 2014; Freeman, 2013). As pore pressure rises above the hydrostatic gradient it can reduce the effective stress for failure.

INTERPRETATIONS AND DISCUSSION

We define a mechanical stratigraphy for the rocks encountered in the MH-2 Project HOTSPOT drillhole that is based on the lithology, fracture and fault density, bulk-rock density data (Figs. 3, 6, 8, and 15) combined with static elastic properties and rock strength from unconfined uniaxial compressive strength tests (Kessler, 2014), and wireline log signatures. Three horizons exhibit high fault density, five zones of moderate fracture density, and one zone devoid of fractures. The lowest highly fractured and faulted unit from 1700 m and lower is a combination of hydrothermally altered fault breccia and gouge. Fracture density increases significantly in the strong, brittle units (Figs. 3 and 6), particularly at the base of the stiff units just above the top of a compliant unit, fault, and altered zone. Fracture stratigraphy and mechanical stratigraphy are a function of rock type and mimic the lithology over the ZOI. The zone exhibits a significant number of faults, but few fractures, from 1500 to 1600 m; a fractured and faulted section is encountered from 1300 to 1400 m md. It was suggested (Kessler, 2014) that the fluid inflow at 1745 m md occurs along an altered and fractured basalt horizon below a thin seal, and above this seal is a fractured region.

The relationships derived from the Bostic-1A well indicate as much as 2700 m of offset along the basin-bounding faults (Malde, 1991; Wood and Clemens, 2002), and the gravity data suggest that the Mountain Home area is on a region of west-northwest-trending faults (Fig. 16). We would expect some of that offset to be expressed on the faults in the MH-2 borehole. The original interpretation of the potential field geophysics for the MH-2 borehole region was that the drillhole was located on the southwest flank of a 300°-trending gravity high (Shervais et al., 2011, 2014a), slightly oblique to the 310°–315°-trending faults at the surface. Reinterpretation of the gravity and aeromagnetic data and new

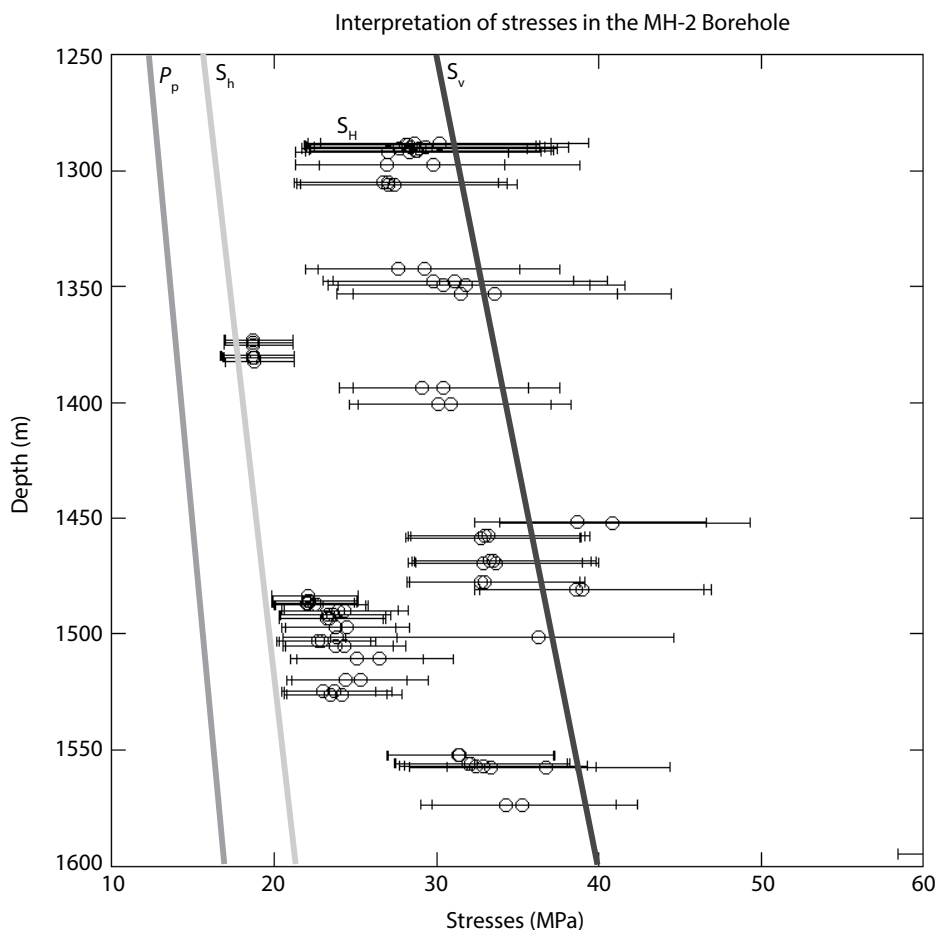


Figure 15. Calculated values of the maximum horizontal stresses, and models for stresses as a function of depth in the MH-2 borehole (see text for explanation of variables). Simple stress-depth model for $S_v > S_H > S_h$ using the borehole breakout fracture widths to estimate the magnitude of S_H . The measured magnitude of S_H will be $\leq S_v$ and the rocks would be at or near a critical stress for fault failure.

data (Glen and Bouligand, 2014) indicate the presence of a well-defined 290°-trending gravity high, the crest of which might be offset by north- to northwest-trending features, and the aeromagnetic signature indicates the presence of short-wavelength north-trending anomalies (Glen and Bouligand, 2014).

Local variations of in situ stresses are a function of the local geologic environment (Heidlebach et al., 2008) and can be due to deflections or transitions at distinct geologic boundaries, including faults, intrusive contacts, or other abrupt changes in mechanical properties of rocks (Sahara et al., 2014; Seithel et al., 2015). Local stress variations can also occur where there are structures or geologic horizons significantly weaker than the surrounding rocks that decouple a site from the regional stress field (such as salt or shale horizons or melt) and there can also be localized sources of body forces to create stresses, such as produced by thermal contraction or expansion, local variations in rock density, topography, mechanical work done by intrusions or diapirs, or by the removal of material by magma or salt flow or dissolution. If the edge of the west-northwest-trending gravity high is a result of normal faulting (Shervais et al.,

2002; Varriale, 2016), the 047° S_H orientation values and magnitudes determined in this study produce oblique right-lateral shear couples on north-trending normal faults (Fig. 16).

Using the fault model and stress orientations and relative magnitudes, we suggest possible orientations for critically stressed faults at depth. The shear stress (τ) and normal stress (σ_n) acting on a fault or fracture plane is defined as critically stressed when:

$$\tau/\sigma_n > 0.6, \quad (7)$$

assuming that cohesion is ≈ 0 for highly fractured rocks. The data for the MH-2 core show that the rocks exhibit a considerable density of fractures, and the borehole image log data suggest that these fractures are in 4–5 concentrated orientations (Fig. 3H). The northeast trend of S_H would most likely activate the northeast- or northwest-trending surfaces. If our assumption that the dominant stress state here is that of normal and/or oblique faulting, then a simple Andersonian stress state (Anderson, 1951) may exist, where $S_v > S_H > S_h$ to $S_v \approx S_H > S_h$.

Variability and uncertainty is high in the S_H magnitude calculations, but we see that they generally plot below the magnitude of S_v (Fig. 15).

In the horizons where S_H approaches the magnitude of S_v we suggest that the stresses in the borehole support a structural model that incorporates oblique normal and/or strike-slip failure on faults (Zoback, 1989) around MH-2 that are optimally oriented for failure in the intersection zone of north- and west-northwest-trending faults (Fig. 16).

Blind geothermal systems (those that lack surface manifestation of high heat flow, such as the presence of fumaroles, hot springs, or hydrothermally altered rocks at the surface) in the western United States are commonly associated with structural complexities where fault tips, stepovers, and intersections or zones of fault splays create enhanced permeability in the complexly faulted zones (Ward et al., 1981; Faulds et al., 2011, 2016; Faulds and Hinz, 2015). We suggest that the vertically varying stress regime from normal to strike-slip regimes creates a structurally complex zone transverse to the trend of the SRP volcanic complex at depth, and this serves to localize high-temperature water encountered at the bottom of the drillhole.

At the base of the MH-2 borehole, elevated pore pressures are likely present due to the flow of thermal waters to the surface (Freeman, 2013; Shervais et al., 2014a), and the presence

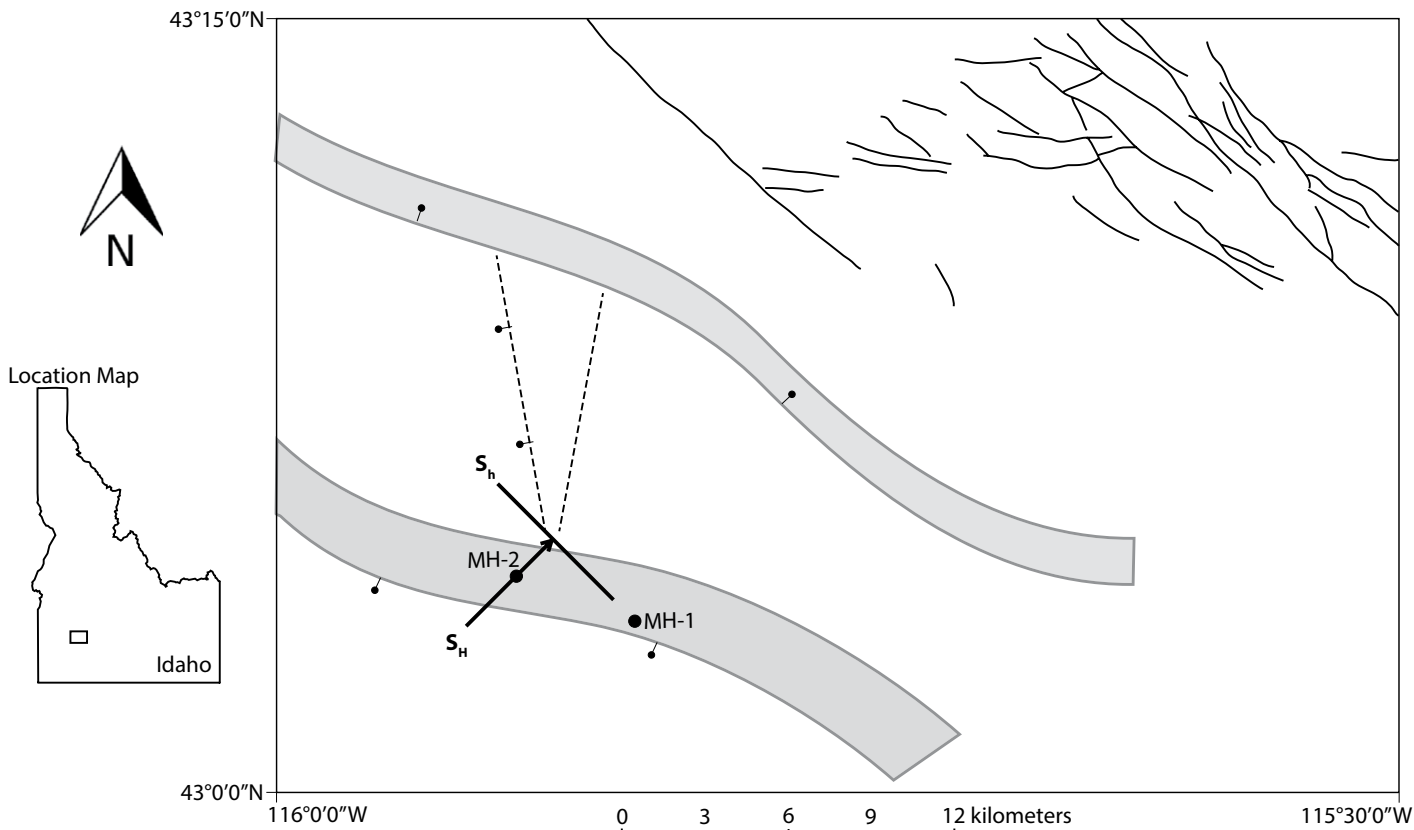


Figure 16. Map view of the schematic setting of the faults and in situ stresses in the MH-2 area. The shaded regions are the approximate locations of steep gradients in the residual gravity data (Shervais et al., 2014a; Glen and Bouligand, 2014). Dashed lines represent the range of orientations for possible normal-oblique slip faults that may cut the gravity high, interpreted to be a horst block of lower basalts.

of borehole breakouts indicates that stress anisotropy is high enough to preferentially strain the borehole to a depth of 1594 m. Elevated pore pressure would promote failure, and intermediate faulting mechanisms could increase the range of orientations for critically stressed faults and fractures that could increase the total fracture permeability in the reservoir. This phenomenon has been observed in other fractured geothermal reservoirs, for example, Dixie Valley and Desert Peak in Nevada (Faulds et al., 2011), and other reservoir types, for example, Yucca Mountain, the North Sea Chalk, the Timor Sea, and the Visund oil and gas field in the North Sea (Kucks, 1999; Zoback, 2010; Hennings et al., 2012).

The setting of the MH-2 borehole with respect to the regional tectonic setting may contribute to the N47°–67°E orientation of S_H . The borehole is near the change in orientation of the Snake River Plain, slightly north of the northern Basin and Range stress or deformation province as variably described by Zoback (1989), Zoback and Zoback (1989), Bennett et al. (1999, 2003) and Payne et al. (2012) (Fig. 17). Some Quaternary deformation is manifested on either side of the western SRP in the form of normal faults and there is essentially no seismicity in the area (Fig. 17), and analyses of global positioning system data suggest that the SRP acts as a coherent block, moving ~3 mm/yr westward (Payne et al., 2012).

The nearest measurements of S_H in the region include those in the extending region north of the SRP (Fig. 17; Pierce and Morgan, 1992; Janecke, 1993; Link and Janecke, 1993) with the S_H in the Big Lost River, Little Lost River, and Lemhi Valleys nearly perpendicular to the MH-2 S_H orientation. Conversely, the MH-2 orientation is 20°–25° clockwise from the orientation in northern Nevada (Zoback, 1989) and the modern velocity vectors described by Bennett et al. (1999).

Due to the absence of perturbations or the very small local perturbations that may be caused by igneous processes or local structural complexities, the stress state at MH-2 may reflect the influences of regional stresses in the western SRP, the northern Basin and Range Province, and the extending area of central Idaho. Payne et al. (2012) indicated that the western SRP behaves as an intact block along with the Owyhee Plateau, moving westward. If we call on a local source for the stress variations at MH-2, this would imply that the modern stress and strain in the area are not coaxial, and some internal deformation occurs at depth in the western SRP that is not manifested at the surface. This deformation might be in the form of obliquely opening dikes, or slip along faults, as proposed here.

In the regional context, the MH-2 stress data and the proposed faults in the subsurface may be a manifestation of the northernmost part of the western Great Basin stress and velocity fields (Zoback, 1989; Bennett et al., 2003; Faulds et al., 2016; Fig. 17) that continues into northern Idaho north of the SRP and easternmost Oregon. This interpretation implies that the north-northeast-trending S_H in the extending northern Nevada region continues into southwest Idaho, and is superposed on the western SRP (Fig. 17), creating a blind tectonic regime. The dominant trend of the Basin and Range structures north and south of the western SRP is north-south, and the oblique orientation of the stresses and their magnitudes (Zoback, 1989) are consistent with mixed-mode slip on the faults (Hammond and Thatcher, 2004). This extension is clearly observed in the geologic record (Anders et al., 1989; Pierce and Morgan, 1992; Janecke, 1992) and geodetically (Payne et al., 2012). Superposition of the SRP volcanic complex on the actively extending region yields a surficially quiet faulting regime that masks complex extensional processes at depth (see Rodgers et al., 2002).

CONCLUSIONS

We examined the lithological, fracture, and stress data from the MH-2 borehole in the SRP (Idaho), where artesian thermal waters flowed from near the base of the borehole from a depth of 1745 m. Analyses of the lithologies in the core reveal the presence of 5 lithologic units arranged in 42 horizons 1–40 m thick in the interval from 1280 to 1820 m md. The units are grouped into 9 mechanical sequences, where stiff, strong basalts exhibit high densities of brittle narrow fractures and faults, whereas the weak breccia and altered zones of basalt exhibit few fractures. Fault dips and slip rake angles vary from dip slip to strike slip, with no systematic distribution with depth. The potential geothermal reservoir is capped by a compliant viscoplastic unit that could arrest fracture propagation.

The stress data and the amount of apparent offset in the borehole are strong indications that the MH-2 borehole penetrated a complex structural environment at the southeastern end of the western SRP. In situ stress measurements were determined from 1280 m to 1594 m md, and indicate an S_H orientation of 047°–067°. Estimation of stress magnitudes from the size of the borehole breakouts and unconfined strength measurements are consistent with a normal fault stress state with a significant component of strike-slip motion. We suggest that the MH-2 hole drilled the flank of a steep-sided gravity high, perhaps offset by north-trending oblique-slip normal faults in the middle of the southeastern

part of the western SRP. The orientation of S_H at the MH-2 borehole reflects either local second or third order complexities along the edge of the mid-plain gravity high, or represents the northern continuation of the northern Nevada deforming zone. This region of extension is under the volcanic complex, and continues into central and west-central Idaho. Faults oriented in this direction with normal motion down to the southeast are consistent with the stress orientations and magnitudes in our geomechanical model of normal and strike-slip movement. The map-scale setting indicates that north-northwest-trending faults may be present, and the small faults seen in the core reflect normal-oblique slip.

APPENDIX 1. TERZAGHI CORRECTION AND WEIGHTING FOR FRACTURE DATA

For a borehole that intersects a set of dipping fractures (Appendix Fig. A1) fracture densities as defined by the number of fractures per unit distance will be biased because of the angle between the drillhole and the fracture. Here, δ = minimum angle between the fracture planes and drillhole. The true spacing of fracture set is given by

$$D = D' \sin \delta = D' (1/W), \quad (1)$$

where D' = apparent spacing along a traverse oriented at an angle δ (Φ γυρεν A.1)

$$\text{Let } R' = 1/D = 1/D' \sin \delta = D' \text{ cosec } \delta \\ = \text{true density of joint population.} \quad (2)$$

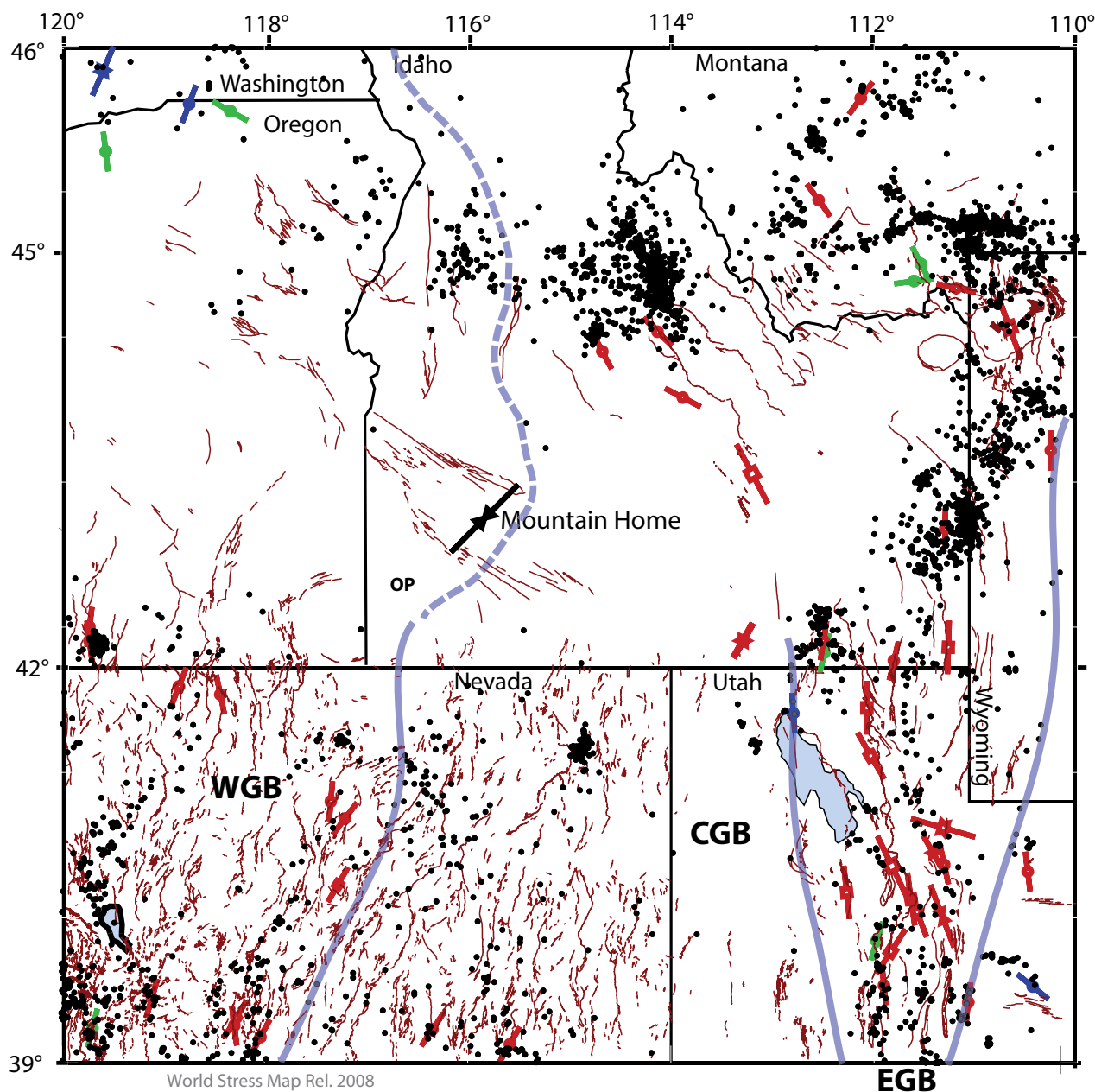
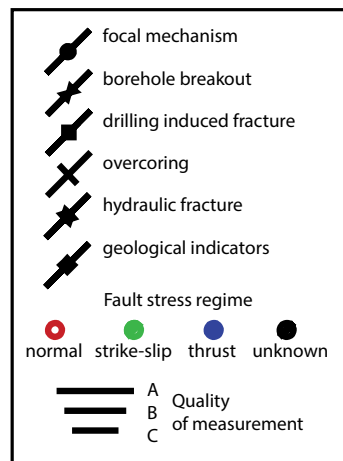
$$\text{Then} \quad W = (1) \text{ cosec } \delta \quad (3)$$

is the weighting factor applied to individual poles in a data population. This weighting function tends to infinity as δ approaches 0 (Priest, 1993), and so a maximum limit for this weighting must be set to prevent unreasonable results. This maximum limit corresponds to a minimum angle, which can be between 1° and 89.9°. We used a maximum weighting factor of 15, which corresponds to a δ of 3.8°.

ACKNOWLEDGMENTS

This work is part of Project HOTSPOT, an ARRA (American Recovery and Reinvestment Act) project funded by U.S. Department of Energy award DE-EE0002848, the International Continental Drilling Program, the U.S. Air Force Air Combat Command, and Utah State University (awards to Shervais), with additional support from the Snake Play Fairway Project (DE-EE0006733, Shervais), and a 2013 ExxonMobil Geoscience Research Grant (to Kessler). The University of Alberta participation was funded primarily through the Natural Sciences and Engineering Research Council of Canada (NSERC) and the Canada Research Chair in Rock Physics to Schmitt. Any use of trade, firm, or product names is for descriptive purposes only and does not imply endorsement by the U.S. Government or any of its agencies. All of the analyses are those of the authors and do not reflect the views or endorsement of the U.S. Government or any of its agencies or contractors. DOSECC Exploration Services LLC, Salt Lake City, Utah, provided expert drilling and coring services, as well as logistical support. We thank Chris Delahunty for expert supervision of the drilling operations and Dennis Nielson for numerous insights into drilling and geothermal systems. Geophysical logging was carried out by the International Continental Drilling Program Operational Support Group, and by commercial logging companies (Pacific Process Systems, Inc., and Southwest Exploration Services, Inc.). We thank the U.S. Air Force 366th Air Combat Command at Mountain Home Air Force Base, including Base Energy Manager Joseph Armstrong and Steve Dumont, for access to the facility and logistical and financial support, and ExxonMobil Corporation for support to Kessler. We also thank Michael Strange, Brady Utley, Digat Vyas, Erica Evans, and Tyler Rasmussen for assistance with logging the core or for field support during coring, and an anonymous reviewer and journal editor A. Weil for constructive reviews.

Figure 17. Map of in situ stresses in the region. Stress data are plotted from the World Stress Map Project (2016); the locations of the active faults in the area are from the Quaternary fault and fold database of the U.S. Geological Survey (2006). Earthquake epicenters ($n = 4311$) from 1960 to the present are from the U.S. Geological Survey National Earthquake Information Center (2016) database. The 047° azimuth of the S_H (see text) in the MH-2 borehole are oriented 20° – 45° clockwise from the S_H orientations in northern Nevada. Boundaries for regions of comparable stress, fault orientations, or global positioning system-determined velocity field (modified from Bennett et al., 2003; Payne et al., 2012) are marked by blue lines. EGB—eastern Great Basin regime, which includes the Intermountain Seismic Belt; CGB—central Great Basin regime, with north-trending normal faults and westward motion; WGB—western Great Basin east-northeast-trending faults, with west-northwest-trending stresses and velocity field; OP—Owyhee Plateau.



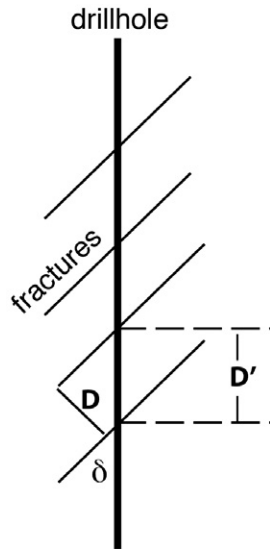


Figure A1. Schematic diagram of a vertical borehole and dipping fracture set defining the terms used in defining a Terzaghi weighting factor.

REFERENCES CITED

- Anders, M.H., Geissman, J.W., Piety, L.A., and Sullivan, J.T., 1989, Parabolic distribution of circum-eastern Snake River Plain seismicity and latest Quaternary faulting: Migratory pattern and association with the Yellowstone hotspot: *Journal of Geophysical Research*, v. 94, p. 1589–1621, doi: 10.1029/JB094iB02p01589.
- Anderson, E.M., 1951, Dynamics of faulting and dyke formation with application to Britain: New York, Hafner Publishing Company, 206 p.
- Arney, B.H., Goff, F., and Harding Lawson Associates, 1982, Evaluation of the hot dry rock geothermal potential of an area near Mountain Home Idaho: Los Alamos National Laboratory Report LA-9365-HDR, 65 p.
- Arney, B.H., Gardner, J.N., and Belloni, S.G., 1984, Petrographic analysis and correlation of volcanic rocks in Bostic 1-A well near Mountain Home, Idaho: Los Alamos National Laboratory Report LA-9966-HDR, 29 p.
- Atkinson, T.A., 2015, Geochemical characterization of the Mountain Home geothermal system [M.S. thesis]: Logan, Utah State University, 105 p., <http://digitalcommons.usu.edu/etd/4599/>.
- Avigad, D., Baer, G., and Heimann, A., 1998, Block rotation and continental extension in the central Aegean Sea: Palaeomagnetic and structural evidence from Tinos and Mykonos (Cyclades): *Earth and Planetary Science Letters*, v. 157, p. 23–40, doi:10.1016/S0012-821X(98)00024-7.
- Barker, C., 1972, Aquathermal pressure—Role of temperature in development of abnormal pressure zones: *American Association of Petroleum Geologists Bulletin*, v. 56, p. 2068–2071.
- Barton, C.A., Zoback, M.D., and Burns, K.L., 1988, In situ stress orientation and magnitude at the Fenton geothermal site, New Mexico, determined from wellbore breakouts: *Geophysical Research Letters*, v. 15, p. 467–470, doi:10.1029/GL015i005p00467.
- Barton, C.A., Zoback, M.D., and Moos, D., 1995, Fluid flow along potentially active faults in crystalline rocks: *Geology*, v. 23, p. 683–686, doi:10.1130/0091-7613(1995)023<0683:FFAPAF>2.3.CO;2.
- Bennett, R.A., Davis, J.L., and Wernicke, B.P., 1999, Present-day pattern of Cordilleran deformation in the western United States: *Geology*, v. 27, p. 371–374, doi:10.1130/0091-7613(1999)027<0371:PDPOCD>2.3.CO;2.
- Bennett, R.A., Wernicke, B.P., Niemi, N.A., Friedrich, A.M., and Davis, J.L., 2003, Contemporary strain rates in the northern Basin and Range province from GPS data: *Tectonics*, v. 22, 1008, doi:10.1029/2001TC001355.
- Blackwell, D.D., 2012, Geothermal heat flow map of the U.S.: Dallas, Texas, Southern Methodist University Geothermal Laboratory, 1 p., <http://www.smu.edu/~media/Site/Dedman/Academics/Programs/Geothermal%20Lab/Graphics/SMU2011USHeatFlowMap.aspx?la=en>.
- Blake, K., 2013, Stress analysis for boreholes on Department of Defense lands in the western United States: A study in stress heterogeneity: *Proceedings, 38th Workshop on Geothermal Reservoir Engineering, SGP-TR-198*, 12 p., <https://www.geothermal-energy.org/pdf/IGAstandard/SGW/2013/Blake.pdf>.
- Bonnichsen, B., and Godchaux, M.M., 2002, Late Miocene, Pliocene, and Pleistocene geology of southwestern Idaho with emphasis on basalts in the Bruneau-Jarbridge, Twin Falls, and western Snake River Plain regions, in Bonnichsen, B., et al., eds., *Tectonic and magmatic evolution of the Snake River Plain volcanic province: Idaho Geological Survey Bulletin* 30, p. 233–312.
- Bonnichsen, B., Leeman, W.P., Horjo, N., McIntosh, W.C., and Godchaux, M.M., 2008, Miocene Silicic volcanism in southwestern Idaho: Geochronology, geochemistry, and evolution of the central Snake River Plain: *Bulletin of Volcanology*, v. 70, p. 315–342, doi:10.1007/s00445-007-0141-6.
- Boulton, S.J., and Robertson, A.H., 2008, The Neogene–recent Hatay graben, south central Turkey: Graben formation in a setting of oblique extension (transtension) related to post-collision tectonic escape: *Geological Magazine*, v. 145, p. 800–821, doi:10.1017/S0016756808005013.
- Breckenridge, R.M., Lewis, R.S., Adema, G.W., and Weisz, D.W., 2003, Miocene and younger faults in Idaho: Idaho Geological Survey Map 8, 1 sheet, scale 1:1,000,000.
- Byerlee, J., 1978, Friction of rocks: *Pure and Applied Geophysics*, v. 116, p. 615–626, doi:10.1007/BF00876528.
- Davatzes, N.C., and Hickman, S., 2010, Stress, fracture, and fluid-flow analysis using acoustic and electrical image logs in hot fractures granites of the Coso Geothermal Field, California, in Pöppelreiter, L.M., et al., eds., *Dipmeter and borehole image log technology: American Association of Petroleum Geologists Memoir* 92, p. 1–35, doi:10.1306/13181288M923.
- Delahunty, C., Nielson, D.L., and Shervais, J.W., 2012, Deep core drilling of three slim geothermal holes, Snake River Plains, Idaho: *Geothermal Resources Council Transactions*, v. 36, p. 641–647.
- Delahunty, C., Nielson, D.L., and Shervais, J.W., 2014, Slim hole coring and drilling operations, in Shervais, J.W., and the Project Hotspot Science Team, eds., *Final project report: The Snake River Geothermal Drilling Project—Innovative approaches to geothermal exploration: Department of Energy Geothermal Technology Office Project DE-EE 0002848*, doi:10.2172/1236394.
- Faulds, J.E., and Hinz, N.H., 2015, Favorable tectonic and structural settings of geothermal systems in the Great Basin region, western USA: Proxies for discovering blind geothermal systems, in *Proceedings, World Geothermal Congress 2015: Bochum, Germany, International Geothermal Association*, 6 p., <https://pangea.stanford.edu/ERE/db/WGC/papers/WGC/2015/11100.pdf>.
- Faulds, J.E., Hinz, N.H., Coolbaugh, M.F., Cashman, P.H., Kratt, C., Dering, G., Edwards, J., Mayhew, B., and McLachlan, H., 2011, Assessment of favorable structural settings of geothermal systems in the Great Basin, western USA: *Geothermal Resources Council Transactions*, v. 35, p. 777–783.
- Faulds, J.E., Hinz, N.H., Coolbaugh, M.F., dePolo, C.M., Siler, D.L., Shevenell, L.A., Hammond, W.C., Kreemer, C., and Queen, J.H., 2016, Discovering geothermal systems in the Great Basin region: An integrated geologic, geochemical, and geophysical approach for establishing geothermal play fairways: *Proceedings, 41st Workshop on Geothermal Reservoir Engineering, SGP-TR-209*, 15 p., <https://pangea.stanford.edu/ERE/db/GeoConf/papers/SGW/2016/Faulds1.pdf>.
- Freeman, T.G., 2013, Evaluation of the geothermal potential of the Snake River Plain, Idaho, based on three exploration holes [M.S. thesis]: Logan, Utah State University, 103 p., <http://digitalcommons.usu.edu/etd/2020/>.
- Glen, J.M.G., and Bouligand, C., 2014, Potential field studies, in Shervais, J.W., and the Project Hotspot Science Team, eds., *Final project report: The Snake River Geothermal Drilling Project—Innovative approaches to geothermal exploration: Department of Energy Geothermal Technology Office Project DE-EE 0002848*, p. 5-1–5-30, <http://www.osti.gov/scitech/biblio/1236394>.
- Glen, J.M.G., and Ponce, D.A., 2002, Large-scale fractures related to inception of the Yellowstone hotspot: *Geology*, v. 30, p. 647–650, doi:10.1130/0091-7613(2002)030<0647:LSFRTI>2.0.CO;2.
- Godchaux, M., Bonnichsen, B., and Jenks, M.D., 1992, Types of phreatomagmatic volcanoes in the western Snake River Plain, Idaho, USA: *Journal of Volcanology and Geothermal Research*, v. 52, p. 1–25, doi:10.1016/0377-0273(92)90130-6.
- Gough, D.I., and Bell, J.S., 1982, Stress orientations from borehole wall fractures with examples from Colorado, east Texas, and northern Canada: *Canadian Journal of Earth Sciences*, v. 19, p. 1358–1370, doi:10.1139/e82-118.
- Hammond, W.C., and Thatcher, W., 2004, Contemporary tectonic deformation of the Basin and Range province, western United States: 10 years of observation with the global positioning system: *Journal of Geophysical Research*, v. 109, B08403, doi:10.1029/2003JB002746.
- Heidbach, O., Tingay, M., Barth, A., Reinecker, J., Kurfel, D., and Müller, B., 2008, The world stress map database release 2008: doi:10.1594/GFZ.WSM.Rel2008.
- Hennings, P., Allwardt, P., Paul, P., Zahm, C., Reid, R., Alley, H., Kirschner, R., Lee, B., and Hough, B., 2012, Relationship between fractures, fault zones, stress, and reservoir productivity in the Suban gas field, Sumatra, Indonesia: *American Association of Petroleum Geologists Bulletin*, v. 96, p. 753–772, doi:10.1306/08161109084.
- Howard, K.A., Shervais, J.W., and McKee, E.H., 1982, Canyon-filling lavas and lava dams on the Boise River, Idaho, and their significance for evaluating downcutting during the last two million years, in Bonnichsen, B., and Breckenridge, R.M., eds., *Cenozoic geology of Idaho: Idaho Bureau of Mines Geology Bulletin* 26, p. 629–641.
- Hughes, S.S., Wetmore, P.H., and Casper, J.L., 2002, Evolution of Quaternary tholeiitic basalt eruptive centers on the eastern Snake River Plain, Idaho, in Bonnichsen, B., et al., eds., *Tectonic and magmatic evolution of the Snake River Plain volcanic province, Idaho: Idaho Geological Survey Bulletin* 30, p. 363–385.
- Jaeger, J.C., and Cook, N.G.W., 1979, *Fundamentals of rock mechanics* (third edition): London, Chapman and Hall, 593 p.
- Janecke, S.U., 1992, Kinematics and timing of three superposed extensional systems, east central Idaho: Evidence for an Eocene tectonic transition: *Tectonics*, v. 11, p. 1121–1138, doi:10.1029/92TC00334.
- Janecke, S.U., 1993, Structures in segment boundary zones of the Lost River and Lemhi faults, east-central Idaho: *Journal of Geophysical Research*, v. 98, p. 16,223–16,238, doi:10.1029/93JB01431.
- Jenks, M.D., and Bonnichsen, B., 1989, Subaqueous basalt eruptions into Pliocene Lake Idaho, Snake River Plain, Idaho, in Chamberlain, V.E., et al., eds., *Guidebook to the geology of northern Idaho: Idaho Geological Survey Bulletin* 28, p. 17–34.
- Kessler, J.A., 2014, In-situ stress and geology from the MH-2 borehole, Mountain Home, Idaho: Implications for geothermal exploration from fractures, rock properties, and geomechanics [Ph.D. thesis]: Logan, Utah State University, 160 p., <http://digitalcommons.usu.edu/etd/3966/>.
- Kinslow, R., Hass, B., Maddi, P., and Bakane, P., 2012, Development overview of geothermal resources in Kilauea East rift zone: *Geo-Heat Center Bulletin*, August, p. 9–17.
- Knott, T.R., Branney, M.J., Reichow, M.K., Finn, D.R., Coe, R.S., Storey, M., Barford, D., and McCurry, M., 2016, Mid-Miocene record of large-scale Snake River-type explosive volcanism and associated subsidence on the Yellowstone hotspot track: *The Cassia Formation of Idaho, USA: Geological Society of America Bulletin*, v. 128, p. 1121–1146, doi:10.1130/B31324.1.
- Kucks, R.P., 1999, Bouguer gravity anomaly data grid for the conterminous US: U.S. Geological Survey Digital Data Series DDS-9, <https://mrdata.usgs.gov/metadata/usgrvbug.faq.html>.
- Lachmar, T.L., Freeman, T., Shervais, J.W., and Nielson, D.E., 2012, Preliminary results: Chemistry and thermometry of geothermal water from MH-2B test well: *Geothermal Resources Council Transactions*, v. 36, p. 689–692.
- Lewis, R.E., and Stone, M.A.J., 1988, Geohydrologic data from a 4,403-foot geothermal test hole, Mountain Home Air Force Base, Elmore County, Idaho: U.S. Geological Survey Open-File Report 88-166, 30 p.
- Link, P.K., and Janecke, S.U., 1999, Geology of east-central Idaho: Geologic roadlogs for the Big and Little Lost River, Lemhi, and Salmon River Valleys, in Hughes, S.S., and Thackray, G.D., eds., *Guidebook to the geology of eastern Idaho: Pocatello, Idaho Museum of Natural History*, p. 295–334.
- Luo, X., and Vasseur, G., 1992, Contributions of compaction and aquathermal pressure to geopressure and the

- influence of environmental conditions: *American Association of Petroleum Geologists Bulletin*, v. 76, p. 1550–1559.
- Malde, H.E., 1991, Quaternary geology and structural history of the Snake River Plain, Idaho and Oregon, *in* Morrison, R.B., ed., *Quaternary nonglacial geology: Conterminous United States*: Boulder, Colorado, Geological Society of America, *Geology of North America*, v. K2, p. 251–281, doi:10.1130/DNAG-GNA-K2.251.
- McCurry, M., and Rodgers, D.W., 2009, Mass transfer along the Yellowstone hotspot track I: Petrologic constraints on the volume of mantle-derived magma: *Journal of Volcanology and Geothermal Research*, v. 188, p. 86–98, doi:10.1016/j.jvolgeores.2009.04.001.
- McCurry, M., Hayden, K., Morse, L., and Mertzman, S., 2008, Genesis of post-hotspot, A-type rhyolite of the Eastern Snake River Plain volcanic field by extreme fractional crystallization of olivine tholeiite: *Bulletin of Volcanology*, v. 70, p. 361–383, doi:10.1007/s00445-007-0143-4.
- McIntyre, D.H., 1979, Preliminary description of Anschutz Federal No. 1 drill hole, Owyhee County, Idaho: U.S. Geological Survey Open-File Report 79-651, 15 p.
- Moos, D., and Zoback, M.D., 1990, Utilization of observations of well bore failure to constrain the orientation and magnitude of crustal stresses—Applications to continental, deep-sea drilling, and ocean drilling program boreholes: *Journal of Geophysical Research*, v. 95, p. 9305–9325, doi:10.1029/JB095iB06p09305.
- Morin, R.H., Carleton, G.B., and Poirier, S., 1997, Fractured-aquifer hydrogeology from geophysical logs; the Passaic Formation, New Jersey: *Ground Water*, v. 35, p. 328–338, doi:10.1111/j.1745-6584.1997.tb00090.x.
- Nielson, D.L., and Shervais, J.W., 2014, Conceptual model for Snake River Plain geothermal systems: *Proceedings, 39th Workshop on Geothermal Reservoir Engineering, SGP-TR-202*, 7 p., <https://pangea.stanford.edu/ERE/db/GeoConf/papers/SGW/2014/Nielson.pdf>.
- Nielson, D.L., Delahunty, C., and Shervais, J.W., 2012, Geothermal systems in the Snake River Plain, Idaho, characterized by the Hotspot Project: *Geothermal Resources Council Transactions*, v. 36, p. 727–730.
- Nielson, D.L., Blackwell, D.D., Frone, Z., and Shervais, J.W., 2014, Borehole thermal logging, *in* Shervais, J.W., and the Project Hotspot Science Team, eds., *Final project report: The Snake River Geothermal Drilling Project—Innovative approaches to geothermal exploration*: Department of Energy Geothermal Technology Office Project DE-EE 0002848, doi:10.2172/1236394.
- Payne, S.J., McCaffrey, R., King, R.W., and Katterhorn, S.A., 2012, A new interpretation of deformation rates in the Snake River Plain and adjacent basin and range regions based on GPS measurements: *Geophysical Journal International*, v. 189, p. 101–122, doi:10.1111/j.1365-246X.2012.05370.x.
- Pierce, K.L., and Morgan, L.A., 1992, The track of the Yellowstone hotspot: Volcanism, faulting, and uplift, *in* Link, P.K., et al., eds., *Regional geology of eastern Idaho and western Wyoming*: Geological Society of America *Memoir* 179, p. 1–54, doi:10.1130/MEM179-p1.
- Pierce, K.L., Morgan, L.A., and Saltus, R.W., 2002, Yellowstone plume head: Postulated tectonic relations to the Vancouver slab, continental boundaries, and climate, *in* Bonnichsen B., et al., eds., *Tectonic and magmatic evolution of the Snake River Plain volcanic province*: Idaho Geological Survey *Bulletin* 30, p. 5–33.
- Pöppelreiter, M., Garcia-Carballido, C., and Kraaijveld, M., 2010, Borehole image log technology: Application across the exploration and production cycle, *in* Pöppelreiter, M., et al., eds., *Dipmeter and borehole image log technology*: American Association of Petroleum Geologists *Memoir* 82, p. 1–13, doi:10.1306/13181274M923406.
- Priest, S.D., 1993, Discontinuity analysis for rock engineering: London, Chapman and Hall, 473 p.
- Rodgers, D.W., Ore, H.T., Bobo, R.T., McQuarrie, N., and Zentner, N., 2002, Extension and subsidence of the eastern Snake River Plain, Idaho, *in* Bonnichsen, W., et al., eds., *Tectonic and magmatic evolution of the Snake River Plain volcanic province*: Idaho Geological Survey *Bulletin* 30, p. 121–155.
- Rouby, D., Fossen, H., and Cobbold, P.R., 1996, Extension, displacement, and block rotation in the larger Gulfaks area, northern North Sea: Determined from map view restoration: *American Association of Petroleum Geologists Bulletin*, v. 80, p. 875–890.
- Ruez, D.R., Jr., 2009, Framework for stratigraphic analysis of Pliocene fossiliferous deposits at Hagerman Fossil Beds National Monument, Idaho: *Rocky Mountain Geology*, v. 44, no. 1, p. 33–70, doi:10.2113/grocky.44.1.33.
- Sahara, D.P., Schoenball, M., Kohl, T., and Müller, B.I.R., 2014, Impact of fracture networks on borehole breakout heterogeneities in crystalline rock: *International Journal of Rock Mechanics and Mining Sciences*, v. 71, p. 301–309, doi:10.1016/j.ijrmms.2014.07.001.
- Schmitt, D.R., Holme, L., and MacKinnon, J.S., 1992, Applications of real time digital acquisition of ultrasonic borehole televiewer data on a personal computer: *Review of Scientific Instruments*, v. 63, p. 3767–3772, doi:10.1063/1.1143268.
- Schmitt, D.R., Currie, C.A., and Zhang, L., 2012a, Crustal stress determination from boreholes and rock cores: Fundamental principles: *Tectonophysics*, v. 580, p. 1–26, doi:10.1016/j.tecto.2012.08.029.
- Schmitt, D.R., Liberty, L.M., Kessler, J.A., Kück, J., Kofman, R., Bishop, R., Shervais, J.W., Evans, J.P., and Champion, D.E., 2012b, The ICDP Snake River Geothermal Drilling Project: Preliminary overview of borehole geophysics: *Geothermal Resources Council Transactions*, v. 36, p. 1017–1022.
- Schmitt, D.R., Lee, M.D., Liberty, L.M., Kessler, J.E., Kück, J., Kofman, R., Bishop, R., Shervais, J.W., Evans, J.P., and Champion, D.E., 2014, Borehole geophysical logging, *in* Shervais, J.W., and the Project Hotspot Science Team, eds., *Final project report: The Snake River Geothermal Drilling Project—Innovative approaches to geothermal exploration*: Department of Energy Geothermal Technology Office Project DE-EE 0002848.
- Schultz, R.A., 1995, Limits on strength and deformation properties of jointed basaltic rock masses: *Rock Mechanics and Rock Engineering*, v. 28, p. 1–15, doi:10.1007/BF01024770.
- Seithel, R., Steiner, U., Muller, B., Hecht, C., and Kohl, T., 2015, Local stress anomaly in the Bavarian Molasse Basin: *Geothermal Energy*, v. 3, doi:10.1186/s40517-014-0023-z.
- Shervais, J.W., 2014, Site characterization and selection, *in* Shervais, J.W., and the Project Hotspot Science Team, eds., *Final project report: The Snake River Geothermal Drilling Project—Innovative approaches to geothermal exploration*: Department of Energy Geothermal Technology Office Project DE-EE 0002848, doi:10.2172/1236394.
- Shervais, J.W., and Hanan, B.B., 2008, Lithospheric topography, tilted plumes, and the track of the Snake River–Yellowstone Hotspot: *Tectonics*, v. 27, TC5004, doi:10.1029/2007TC002181.
- Shervais, J.W., and Vetter, S.K., 2009, High-K alkali basalts of the western Snake River Plain: Abrupt transition from tholeiitic to mildly alkaline plume-derived basalts: *Journal of Volcanology and Geothermal Research*, v. 188, p. 141–152, doi:10.1016/j.jvolgeores.2009.01.023.
- Shervais, J.W., Shroff, G., Vetter, S.K., Matthews, S., Hanan, B.B., and McGee, J.J., 2002, Origin and evolution of the western Snake River Plain: Implications from stratigraphy, faulting, and the geochemistry of basalts near Mountain Home, Idaho, *in* Bonnichsen, B., et al., eds., *Tectonic and magmatic evolution of the Snake River Plain volcanic province*: Idaho Geological Survey *Bulletin* 30, p. 343–361.
- Shervais, J.W., Kauffman, J.D., Gillerman, V.S., Othberg, K.L., Vetter, S.K., Hobson, V.R., Zarnetske, M., Cooke, M.F., Matthews, S.H., and Hanan, B.B., 2005, Basaltic volcanism of the central and western Snake River Plain: A guide to field relations between Twin Falls and Mountain Home, Idaho, *in* Pederson, J., and Dehler, C.M., eds., *Interior western United States: Geological Society of America Field Guide* 6, p. 27–52, doi:10.1130/2005.fl.d006(02).
- Shervais, J.W., et al., 2011, Hotspot: The Snake River Geothermal Drilling Project—An overview: *Geothermal Resources Council Transactions*, v. 35, p. 995–1003.
- Shervais, J.W., et al., 2012, Hotspot: The Snake River Geothermal Drilling Project—Initial report: *Geothermal Resources Council Transactions*, v. 36, p. 767–772.
- Shervais, J.W., et al., 2013, First results from HOTSPOT: The Snake River Plain Scientific Drilling Project, Idaho: U.S.A.: *Scientific Drilling*, v. 15, p. 36–45, doi:10.5194/sd-15-36-2013.
- Shervais, J.W., and the Project Hotspot Science Team, eds., 2014a, Final project report: The Snake River Geothermal Drilling Project—Innovative approaches to geothermal exploration: Department of Energy Geothermal Technology Office Project DE-EE 0002848, 281 p., doi:10.2172/1236394.
- Shervais, J.W., Evans, J.P., Schmitt, D., Christiansen, E.H., and Prokopenko, A., 2014b, Drilling into the track of the Yellowstone hot spot: *Eos (Transactions, American Geophysical Union)*, v. 95, no. 10, p. 85–86, doi:10.1002/2014EO100001.
- Swarbrick, R., 2012, Review of pore-pressure prediction challenges in high-temperature areas: *The Leading Edge*, November, p. 1288–1294.
- Terzaghi, R., 1965, Sources of error in joint surveys: *Geotechnique*, v. 15, p. 287–304, doi:10.1680/geot.1965.15.3.287.
- Trench, D., 2008, The termination of the Basin and Range province into a clockwise rotating region of transtension and volcanism, central Oregon [M.S. thesis]: Corvallis, Oregon State University, 64 p.
- U.S. Geological Survey, 2006, Quaternary fault and fold database for the United States: <http://earthquakes.usgs.gov/regional/qfaults/> (accessed July 2016).
- U.S. Geological Survey National Earthquake Information Center, 2016, <http://earthquake.usgs.gov/earthquakes/browse/>.
- Varriale, J., 2016, The MH-2 core from Project Hotspot: Description, geologic interpretation, and significance to geothermal exploration in the western Snake River Plain, Idaho [M.S. thesis]: Logan, Utah State University, 84 p.
- Walker, J., Wheeler, J., Boersma, A., and Ewen, K., 2014, The smectite to corrensite transition: Preliminary results from the MH-2(B) borehole, western Snake River Plain, Idaho [poster]: *Clay Minerals Society Annual Meeting Abstracts*, p. 231, https://cms2014.tamu.edu/files/ProgramAbstracts_CMS2014_LowResolution.pdf.
- Ward, S.H., Ross, H.P., and Nielson, D.L., 1981, Exploration strategy for high-temperature hydrothermal systems in Basin and Range Province: *American Association of Petroleum Geologists Bulletin*, v. 65, p. 86–102.
- Westaway, R., 1990, Block rotation in western Turkey: 1. Observational evidence: *Journal of Geophysical Research*, v. 95, no. B12, p. 19,857–19,884, doi:10.1029/JB095iB12p19857.
- Wohletz, K.H., and Heiken, G., 1992, *Volcanology and geothermal energy*: Berkeley, University of California Press, 432 p.
- Wood, S., 1994, Seismic expression and geologic significance of a lacustrine delta in Neogene deposits of the western Snake River Plain, Idaho: *American Association of Petroleum Geologists Bulletin*, v. 78, p. 102–121.
- Wood, S.H., and Clemens, D.M., 2002, Geologic and tectonic history of the western Snake River Plain, Idaho and Oregon, *in* Bonnichsen, B., et al., eds., *Tectonic and magmatic evolution of the Snake River Plain volcanic province*: Idaho Geological Survey *Bulletin* 30, p. 69–103.
- World Stress Map Project, 2016, Stress data of the World Stress Map: <http://www.world-stress-map.org/> (accessed March 2016).
- Zemanek, J., Caldwell, R.L., Glenn, E.E., Jr., Holcomb, S.W., Norton, L.J., and Straus, A.J.D., 1969, The borehole televiewer; a new logging concept for fracture location and other types of borehole inspections: *Journal of Petroleum Technology*, v. 25, p. 761–774, doi:10.2118/2402-PA.
- Zhang, P., Slemmons, D.B., and Mao, F., 1991, Geometric pattern, rupture termination and fault segmentation of the Dixie Valley–Pleasant Valley active normal fault system, Nevada, USA: *Journal of Structural Geology*, v. 13, p. 165–176, doi:10.1016/0191-8141(91)90064-P.
- Zoback, M.D., 2010, *Reservoir geomechanics*: New York, Cambridge University Press, 461 p., doi:10.1017/CBO9780511586477.
- Zoback, M.D., Barton, C.A., Castillo, D.A., Finkbeiner, T., Grolimum, B.R., Moos, D.B., Ward, C.D., and Wiprut, D.J., 2003, Determination of stress orientation and magnitude in deep wells: *International Journal of Rock Mechanics and Mining Sciences*, v. 40, p. 1049–1076, doi:10.1016/j.ijrmms.2003.07.001.
- Zoback, M.L., 1989, State of stress and modern deformation of the northern Basin and Range Province: *Journal of Geophysical Research*, v. 94, p. 7105–7128, doi:10.1029/JB094iB06p07105.
- Zoback, M.L., and Zoback, M.D., 1989, Tectonic stress field of the continental United States, *in* Pakiser, L.C., and Mooney, W.D., eds., *Geophysical framework of the continental United States*: Geological Society of America *Memoir* 172, p. 523–540, doi:10.1130/MEM172-p523.

MANUSCRIPT RECEIVED 12 AUGUST 2016

REVISED MANUSCRIPT RECEIVED 13 JANUARY 2017

MANUSCRIPT ACCEPTED 1 MARCH 2017

Printed in the USA